

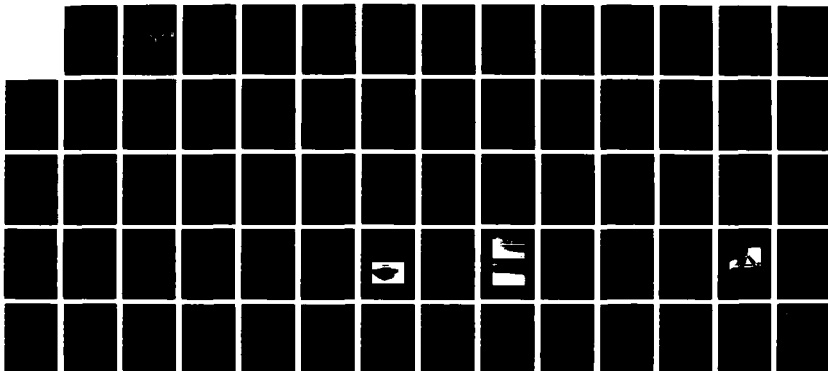
AD-A188 356

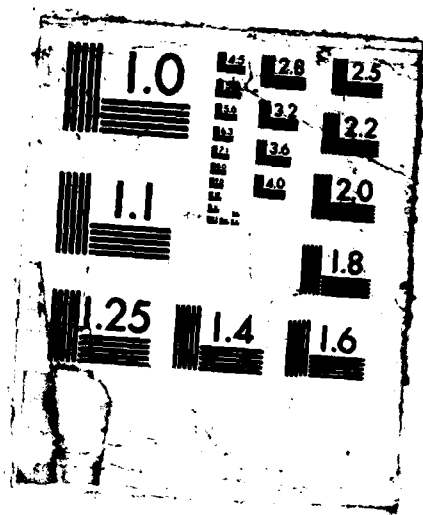
EFFECTS OF WAVES ON THE BOUNDARY LAYER OF A  
SURFACE-PIERCING FLAT PLATE... (U) IOWA INST OF  
HYDRAULIC RESEARCH IOWA CITY F STERN ET AL SEP 87  
IIHR-318 N00014-82-K-0136 F/G 8/3

1/1

UNCLASSIFIED

NL





AD-A188 356

EFFECTS OF WAVES  
ON THE BOUNDARY LAYER  
OF A  
SURFACE-PIERCING FLAT PLATE:  
EXPERIMENT AND THEORY

by

F. Stern, W.S. Hwang, and S.Y. Jaw



DTIC  
-LECTE  
NOV 20 1987  
S D

IIHR Report No. 318

Iowa Institute of Hydraulic Research  
The University of Iowa  
Iowa City, Iowa 52242

September 1987

**DISTRIBUTION STATEMENT A**

Approved for public release;  
Distribution Unlimited

87 11 101

**EFFECTS OF WAVES ON THE BOUNDARY LAYER OF A  
SURFACE-PIERCING FLAT PLATE: EXPERIMENT AND THEORY**

by

**F. Stern, W.S. Hwang, and S.Y. Jaw**

Sponsored by

Office of Naval Research  
Accelerated Research Initiative (Special Focus)  
Program in Ship Hydrodynamics  
Contract No. N00014-83-K-0136

IIHR Report No. 318

Iowa Institute of Hydraulic Research  
The University of Iowa  
Iowa City, Iowa 52242

September 1987

Approved for Public Release: Distribution Unlimited



Accession For	
NTIS CRA&I	<input checked="checked" type="checkbox"/>
DTIC TAB	<input type="checkbox"/>
Unannounced	<input type="checkbox"/>
Justification	
By	
Distribution/	
Availability Codes	
Dist	Avail and/or Special
A-1	

Unclassified

SECURITY CLASSIFICATION OF THIS PAGE (When Data Entered)

REPORT DOCUMENTATION PAGE		READ INSTRUCTIONS BEFORE COMPLETING FORM
1. REPORT NUMBER IIHR Report No. 318	2. GOVT ACCESSION NO.	3. RECIPIENT'S CATALOG NUMBER
4. TITLE (and Subtitle) Effects of Waves on the Boundary Layer of a Surface-Piercing Flat Plate: Experiment and Theory		5. TYPE OF REPORT & PERIOD COVERED Technical Report
		6. PERFORMING ORG. REPORT NUMBER IIHR Report No. 318
7. AUTHOR(s) F. Stern, W.S. Hwang, and S.Y. Jaw		8. CONTRACT OR GRANT NUMBER(s) N00014-83-K-0136
9. PERFORMING ORGANIZATION NAME AND ADDRESS Institute of Hydraulic Research, The University of Iowa, Iowa City, Iowa 52242-1585		10. PROGRAM ELEMENT, PROJECT, TASK AREA & WORK UNIT NUMBERS 432b-002
11. CONTROLLING OFFICE NAME AND ADDRESS Office of Naval Research, 800 N. Quincy Street, Arlington, Virginia 22217		12. REPORT DATE September 1987
		13. NUMBER OF PAGES 64
14. MONITORING AGENCY NAME & ADDRESS (if different from Controlling Office) Office of Naval Research 536 S. Clark Street Chicago, Illinois 60605		15. SECURITY CLASS. (of this report) Unclassified
		15a. DECLASSIFICATION/DOWNGRADING SCHEDULE
16. DISTRIBUTION STATEMENT (of this Report) Approved for Public Release; Distribution Unlimited		
17. DISTRIBUTION STATEMENT (of the abstract entered in Block 20, if different from Report)		
18. SUPPLEMENTARY NOTES		
19. KEY WORDS (Continue on reverse side if necessary and identify by block number) Wave/Boundary-Layer Interaction, 3-D Boundary Layer, Free Surface Ship Boundary Layer		
20. ABSTRACT (Continue on reverse side if necessary and identify by block number) Results are presented from a towing+tank experiment conducted in order to document the effects of waves on the boundary layer of a surface-piercing body. A unique, simple model geometry is utilized which makes it possible to identify and isolate the most important features of the wave-induced effects. Measurements were made of wave profiles as well as detailed boundary-layer velocity profiles for three wave+steepness conditions: zero, medium, and large. The effects of the waves for both the medium+ and large-steepness conditions		

DD FORM 1 JAN 73 1473

EDITION OF 1 NOV 65 IS OBSOLETE  
S/N 0102-LF-014-6601

Unclassified

SECURITY CLASSIFICATION OF THIS PAGE (When Data Entered)

Unclassified

SECURITY CLASSIFICATION OF THIS PAGE (When Data Entered)

are shown to be significant. In particular, the variations of the external-flow piezometric pressure gradients cause acceleration and deceleration phases of the streamwise velocity component and alternating direction of the cross flow which result in large oscillations of the displacement thickness and wall shear stress as compared to the zero steepness condition. The magnitude of these trends increases with increasing wave steepness. Wave-induced separation, which is present under certain conditions in the experiments, and other relevant phenomena are discussed. The measurements are compared and close agreement is demonstrated with results from first-order boundary layer calculations with a symmetry condition approximation for the free-surface boundary conditions.

Unclassified

SECURITY CLASSIFICATION OF THIS PAGE (When Data Entered)

## ABSTRACT

Results are presented from a towing-tank experiment conducted in order to document the effects of waves on the boundary layer of a surface-piercing body. A unique, simple model geometry is utilized which makes it possible to identify and isolate the most important features of the wave-induced effects. Measurements were made of wave profiles as well as detailed boundary-layer velocity profiles for three wave-steepness conditions: zero, medium, and large. The effects of the waves for both the medium- and large-steepness conditions are shown to be significant. In particular, the variations of the external-flow piezometric-pressure gradients cause acceleration and deceleration phases of the streamwise velocity component and alternating direction of the cross flow which result in large oscillations of the displacement thickness and wall-shear stress as compared to the zero-steepness condition. The magnitude of these trends increases with increasing wave steepness. Wave-induced separation, which is present under certain conditions in the experiments, and other relevant phenomena are discussed. The measurements are compared and close agreement is demonstrated with results from first-order boundary-layer calculations with a symmetry-condition approximation for the free-surface boundary conditions.

## ACKNOWLEDGEMENTS

The first author would like to acknowledge and thank Professors Landweber and Patel for their significant contributions to this work. Not only did they suggest the present topic, but they also provided many helpful discussions. In fact, a discussion with the latter led to the present model geometry. Support provided by IIHR's mechanical and electronic shops, especially J. Goss, E. Miller, and J. Cramer, is very much appreciated. This research was sponsored by the Office of Naval Research, Accelerated Research Initiative (Special Focus) Program in Ship Hydrodynamics, under Contract No. N00014-83-K-0136. The Department of Mechanical Engineering and the Graduate College of The University of Iowa provided a large part of the financial support for the second and third authors and the computer funds, respectively.

## LIST OF SYMBOLS

### Alphabetical Symbols

A	wave amplitude
Ak	wave steepness
B	Constant in the logarithmic-overlap law
c	foil chord length
$C_f$	wall-shear-stress magnitude ( $= \tau_w / (1/2 \rho U_c^2)$ )
$C_{pe}$	piezometric-pressure coefficient ( $= P_e / (1/2 \rho U_c^2)$ )
d	foil depth of submergence
g	gravitational acceleration
H	(1) wave height (2) shape parameter ( $= \delta^* / \theta$ )
k	wave number
$K_Q, K_\theta$	pitot-probe calibration coefficients
$L_s$	normalized separation starting point
$P_e$	piezometric pressure
$P_x, P_z$	piezometric-pressure-gradient coefficients
$\frac{-q^2}{2}$	turbulence intensity
Re	Reynolds number
t	foil thickness
$U_e, W_e$	edge velocities in (x, z) directions
U, V, W	velocities in (x, y, z) directions
$U_c$	carriage velocity
$U^+$	inner-law variable ( $= U/U^*$ )
$U^*$	wall-shear velocity ( $= \sqrt{\tau_w / \rho}$ )
$V_e$	edge velocity vector
x, y, z	Cartesian coordinates
$x_s$	separation starting point
$x_{\eta_1}$	x-coordinate at the first wave crest
$y^+$	inner-law variable ( $= yU^* / \nu$ )



## Greek Symbols

$\beta$	wave-front angle
$\delta$	boundary-layer thickness
$\delta^*$	streamwise displacement thickness
$\kappa$	constant in the logarithmic-overlap law
$\lambda$	wavelength
$\mu$	wave-damping factor
$\nu$	kinematic viscosity
$\eta_e$	edge wave elevation
$\eta_1$	first wave crest
$\eta_2$	second wave crest
$\theta$	(1) yaw angle (2) momentum thickness
$\rho$	density
$\tau_w$	wall-shear stress
$\phi$	wave velocity potential

## Subscripts

$e$	edge value, edge of boundary layer
-----	------------------------------------

# TABLE OF CONTENTS

	Page
ABSTRACT.....	1
ACKNOWLEDGEMENTS.....	1
LIST OF SYMBOLS.....	11
I INTRODUCTION.....	1
II. FLOW GEOMETRY AND OVERVIEW OF THE EXPERIMENTAL AND THEORETICAL RESULTS.....	1
III. EXPERIMENTAL EQUIPMENT AND PROCEDURES.....	3
A. Model Geometry.....	3
B. Instrumentation.....	4
C. Calibration.....	5
D. Data-Acquisition System.....	6
E. Experimental Procedure.....	6
1. Wave-Profile Measurements.....	7
2. Velocity Measurements.....	7
F. Experimental Uncertainty.....	7
IV. OUTLINE OF THE COMPUTATIONAL METHOD.....	8
A. Approach.....	8
1. External Flow.....	8
2. Boundary Layer.....	10
B. Calculation Conditions.....	11
V. EXPERIMENTAL AND COMPUTATIONAL RESULTS.....	11
A. Wave Profiles.....	11
B. Wave-Induced Separation.....	13
C. Velocity Profiles.....	16
1. Zero Steepness.....	17
2. Large Steepness.....	19
3. Medium Steepness.....	24
VI. SOME FREE-SURFACE PHENOMENA RELEVANT TO WAVE-INDUCED SEPARATION.....	25
VII. CONCLUDING REMARKS.....	30
REFERENCES.....	32
FIGURES.....	34

## **I. INTRODUCTION**

Experimental information concerning the effects of waves on the boundary layer of a surface-piercing body is extremely limited. Most of the experiments have been performed in towing tanks using various hull forms. Surface shear-stress and pressure distributions and stern and near-wake mean-velocities have been measured. Also, some turbulence measurements have been made in circulating-water channels. Although the results from these studies indicate significant effects due to the presence of the free surface and a dependence on Froude number, the extent of the measurements and Froude number range are limited and they are dependent on hull form such that general conclusions cannot be reached. See Stern (1986) for a more complete review, including theoretical work and references.

This report presents results from a towing-tank experiment conducted in order to document the effects of waves on the boundary layer of a surface-piercing body. A unique, simple model geometry is utilized which makes it possible to identify and isolate the most important features of the wave-induced effects. Furthermore, the flow geometry simulates the Stokes-wave/flat-plate flow field for which calculations were previously performed (Stern, 1986). The capabilities of the computational method of approach are evaluated by making comparisons with the measurements.

## **II. FLOW GEOMETRY AND OVERVIEW OF THE EXPERIMENTAL AND THEORETICAL RESULTS**

A sketch of the experimental model installed in the towing tank (figure 1) is shown in figure 2. The horizontal-submerged foil and vertically-suspended surface-piercing flat plate are attached to a trailer which is towed at constant speed. As will be discussed below, the foil generates waves with properties similar to second-order Stokes waves, although there are some differences due to the downstream plate. Herein, of primary interest is the boundary-layer development on the plate. For large depths, where free-surface effects are negligible, the boundary-layer development is two-dimensional and the flow characteristics are well known. For smaller depths, the boundary-layer development is three-dimensional due to the presence of the free surface and gravity waves, and the flow characteristics need to be documented. For

this purpose, measurements were made of wave profiles as well as detailed boundary-layer velocity profiles for three wave-steepness conditions: zero, medium, and large. The experimental condition is for turbulent flow, except near the leading edge. The longitudinal position of the plate is adjusted so that the plate leading edge coincides with the first wave crest. Velocity profiles were obtained for up to four depths and eight axial locations over one complete wave length. This resembles the practical circumstance for conditions when the wave length is comparable to the ship length and provides experimental information for both the forebody and afterbody regions.

Recently, Stern (1986) performed a theoretical investigation concerning the effects of waves on the boundary layer of a surface-piercing body. Numerical results were presented for both laminar and turbulent flow for the model problem of a combination Stokes-wave/flat-plate. As previously mentioned, this flow field is simulated by the present experimental flow geometry. The first-order boundary-layer equations were solved using an implicit finite-difference method. The calculations demonstrate and quantify the influence of waves on the boundary-layer development. For laminar flow, calculations were made using small-amplitude-wave and more approximate free-surface boundary conditions. For turbulent flow, only the more approximate free-surface boundary conditions were used. Both the external-flow piezometric-pressure gradients and the free-surface boundary conditions were shown to have a significant influence. The former penetrates to a depth of about half the wave length and the latter is confined to a region very close to the free surface. Order-of-magnitude estimates were derived which show that the flow in this region is analogous to the flow in a streamwise corner in that a consistent formulation requires the solution of higher-order viscous-flow equations. Herein, comparisons are made between the measurements and the turbulent-flow calculations.

An outline of the report is as follows. The experimental equipment and procedures are described in Chapter III. In Chapter IV, the computational method is outlined. The experimental and theoretical results are presented and discussed in Chapter V. In Chapter VI, some free-surface phenomena relevant to wave-induced separation which is present in the experiments are discussed. Finally, in Chapter VII, some concluding remarks are provided.

### III. EXPERIMENTAL EQUIPMENT AND PROCEDURES

The experiments were performed in the Iowa Institute of Hydraulic Research (IIHR) towing tank (figure 1). The towing tank is 91.4m long and 3m wide and deep. It is equipped with two instrumented carriages, one driven and one trailer. The towing carriage is cable-driven by a 15hp motor fitted with a transistor-SCR tachometer-feedback speed regulator. The carriage can be towed at speeds up to 6.1m/s with an accuracy of  $\pm 3\%$  for low speeds ( $< 0.3$  m/s),  $\pm 1\%$  for medium speeds (1.25 m/s), and  $< \pm 0.5\%$  for high speeds ( $> 2$  m/s). The carriage is operated from a control panel situated at one end of the tank.

#### A. Model Geometry

The experimental model is shown in figure 2. The horizontal foil (wave-generation mechanism) nearly spans the towing tank and is mounted between end plates which allow for adjustment of the foil's depth of submergence. Downstream of the foil, is the vertically-suspended surface-piercing flat plate. The plate is suspended by an I-beam such that both its lateral and longitudinal positions can be adjusted. The model configuration was designed to generate waves that are as two-dimensional as possible and with as little disturbance by the plate and end plates as possible. Both the foil and plate are attached to a trailer which is towed by the main carriage (see figure 1). This allows for easy access and optimum viewing.

The foil geometry and end plates were designed based on the experiments of Salveser (1966) and Salvesen and von Kerczek (1975). Salvesen (1966) performed similar towing-tank experiments with a horizontal-submerged foil (without the downstream plate) for the purpose of validating his higher-order perturbation wave theory for submerged two-dimensional bodies (Salvesen, 1969). Salvesen reported two-dimensional waves with small damping for about one to two wave lengths. Beyond this distance, the end plates (the end plates extended from the foil's leading to trailing edges) introduced disturbances such that the waves were no longer two-dimensional. In general, the second-order wave profile is in good agreement with the measurements, including both amplitude and wavelength, and shows a great improvement over the linear theory. The wavelengths are about ten percent shorter than the linear-theory predictions. The shape of the waves, both predicted and measured, is

"quite the same" as second-order Stokes waves. In subsequent work (Salvesen and von Kerczek, 1975), the results by perturbation theory were compared with numerical finite-difference solutions for the exact nonlinear inviscid-flow problem. As part of this effort, some additional experiments were performed at the David Taylor Naval Ship Research and Development Center. The same foil geometry was used; however, the experiments were performed in a 12.2m long and 61cm wide and deep tank, which was fully spanned by the foil. In this case, the waves were more uniform across the width of the tank and maintained their shape for longer distances downstream of the foil.

The foil profile (figure 3) is symmetric with chord length  $c = 33.18\text{cm}$  and thickness  $t = 11.44\text{cm}$  ( $t/c = .34$ ). Both the foil and end plates are constructed of aluminum. The end plates extend 2.4 chord lengths downstream of the foil trailing edge. Although the foil angle of attack relative to the uniform flow could be adjusted, in all the experiments conducted the angle of attack was zero.

The flat plate is made of plexiglass with dimensions: 2.5m long, 1.1m high, and 1.27cm thick. L-beams were mounted on the nonmeasurement side of the plate for structural stiffness. The leading edge is wedge shaped to reduce plate-induced wave effects on the measurement side of the plate. A 2 x 2cm grid was painted on the nonmeasurement side of the plate to facilitate the wave-profile measurements. In order to induce turbulent flow, a row of plastic studs with 3.2mm diameter, 1.6mm height, and 9.5mm spacing was fitted on the plate 6cm downstream of the plate leading edge. Some preliminary experiments were made using a similarly constructed aluminum plate (Stern, 1985).

## **B. Instrumentation**

A three-hole yaw probe was used to measure the direction (in vertical planes) and magnitude of the velocity in the three-dimensional boundary layer on the plate. Although this probe does not allow for measurement of the component of velocity normal to the plate, as does a five-hole yaw probe, its dimensions are smaller than the latter, which allows for better resolution of the flow near the wall. In the present experiment, the normal velocity component is small and not of crucial importance. The probe is shown in figure

4. Also shown is the mechanical traverse used to position the probe. The probe could be moved in three directions of a Cartesian coordinate system with the lateral and vertical movements measured by counters with minimum counts of 2mm. The pressure tubes from the probe were connected by plastic tubing to three Validyne pressure transducers. The voltage output from the pressure transducers was sampled, digitized, and recorded by the data-acquisition system to be described subsequently.

### C. Calibration

The pressure transducers were calibrated (voltage vs. pressure) with a Rouse precision manometer. The yaw probe was calibrated in an open-throat wind tunnel. The probe was placed in the working section of the tunnel on an assembly that allowed it to be yawed about the flow direction at any prescribed angle. Since the effects of Reynolds number on calibration are known to be insignificant for wind speeds in excess of 12m/s, the calibration was carried out at a wind speed of 16.53m/s. The reference velocity was determined with a total-head tube.

If the direction of the uniform flow is assumed to be along the x-axis, the yaw angle  $\theta$  and numbering scheme for the pressures  $P_1$ ,  $P_2$ , and  $P_3$  sensed by the probe holes are defined as shown in figure 4.  $P_1$  and  $P_3$  are primarily sensitive to yaw. The following coefficients are defined:

$$K_Q(\theta) = \{P_2 - (P_1 + P_3)/2\} / \{\rho Q^2/2\} \quad (\text{III-1})$$

$$K_\theta(\theta) = \{P_1 - P_3\} / \{P_2 - (P_1 + P_3)/2\} \quad (\text{III-2})$$

where  $\rho$  is the fluid density and  $Q$  the velocity magnitude. The probe was calibrated in the range  $-40^\circ < \theta < 40^\circ$  with 5-degree steps in yaw angle. The calibration coefficients (III-1) and (III-2) were calculated from these measurements and are shown in figure 5. A computer program was developed for data analysis in which third-degree polynomials were fitted by the method of least squares to the calibration results, and values at desired points are obtained by linear interpolation.

The yaw probe was dynamically calibrated in the towing tank at zero yaw angle. This calibration was found to be dependent on depth. Typical results are shown in figure 6 for  $z = (5, 10, 15\text{cm})$ . It is seen that the slope of the calibration line increases with decreasing depth. This is to be expected, since the volume of air in the pitot tube decreases with increasing depth which increases the air pressure; i.e., for the same speed, as the depth increases so does the air pressure (voltage). A steep slope is desirable in order to resolve small velocity differences. At the greatest depth,  $z = 30\text{cm}$ , the calibration was found to be nonlinear such that different calibration lines had to be fitted for the small and large velocity ranges. Also, it was somewhat unstable for the smaller velocity range, due no doubt, to the small pressure difference and slow response time. The standard procedure was to perform a series of measurements for one depth at a time. During each series, the calibration was checked daily.

#### **D. Data-Acquisition System**

The data-acquisition system is a site-dedicated IBM-compatible PC with a data-acquisition interface board. The system features four-channel simultaneous data-sampling capability with a maximum sampling rate of 27,000 samples per second. A generator linearly converts carriage speed to frequency, which is transformed into voltage by a frequency-voltage converter. The sensed pressures from the yaw probe are converted to voltages by the pressure transducers which are sampled simultaneously with the carriage speed through the analog-to-digital converter, digitized, and then read and stored by the computer. A sampling rate of 200 samples/s per channel was used with a time interval of 2s.

#### **E. Experimental Procedure**

Two types of measurements were made: wave profiles and boundary layer velocity profiles. In both cases, a time interval of about 10 minutes between carriage runs was necessary in order for the fluid motion induced by the previous run to be sufficiently damped.



## 1. Wave-Profile Measurements

For prescribed carriage velocity and depth of submergence of the foil, the wave profile on the plate was measured photographically. This was facilitated by the grid painted on the nonmeasurement side of the (plexiglass) plate. For optimum viewing, the pitot-probe traverse was removed for these experiments. For each condition investigated, an average wave steepness was estimated based on the photographs.

## 2. Velocity Measurements

Three wave-steepness conditions were selected for the velocity-profile measurements: zero, medium, and large. In each case, the experiments were conducted at the same carriage velocity ( $U_c = 1.37\text{m/s}$ ) such that, for the latter two cases, the wave length was about 120cm. Measurements were made for up to four depths and eight axial locations. The plate was offset laterally so that the measurement side was at a greater distance from the tank sidewalls than the nonmeasurement side. The plate was positioned longitudinally such that the plate leading edge coincided with the first wave crest. The measurement locations, plate positions, and foil submergence depths are shown in figure 7.

Air-bubble trapping due to the use of a water-air system to transmit pressure to the pressure transducers was avoided by cleaning the connecting tubes with compressed air before each experiment. The measurements were usually made at the same location along the tank (circa.  $3/4$  of the length) where the carriage velocity was nearly constant. Repeatability was checked by typically performing about three measurements per data point.

## F. Experimental Uncertainty

Many factors contribute to error and thus uncertainty in the measurements. Physical errors result due to probe misalignment, the influence of the probe support, wall-proximity effects, probe displacement effects, turbulence effects, and probe geometry. Numerical errors result due to the required interpolations of the calibration coefficients. Here, error estimates will not be provided for each of the above, but rather for the conglomerate. Maximum uncertainties of  $\pm 2.5\%$  and  $\pm 5\%$  are estimated for the U- and W-velocity components, respectively, based on the repeatability of the data.

#### IV. OUTLINE OF THE COMPUTATIONAL METHOD

As discussed above, the flow field of the foil-plate geometry simulates the Stokes-wave/flat-plate flow field for which calculations were previously performed (Stern, 1986). Comparisons will be made between the measurements and the calculations in order to evaluate the capabilities of the computational method of approach. In the following, a brief outline of the computational method of approach is provided. Also, the conditions for the present calculations are stated. The details of the computational method of approach are given by Stern (1986).

##### A. Approach

###### 1. External Flow

Consider the flow field in the vicinity of a surface-piercing, vertical flat plate moving in and at the same speed as a simple two-dimensional periodic-wave train. It is assumed that the plate is sufficiently thin that it generates no waves of its own. Outside of the plate boundary layer, the flow is essentially inviscid and can be represented as a second-order Stokes wave; i.e., the fluid velocity vector  $\mathbf{V}_e$  for coordinates moving with the plate/wave system is given by:

$$\mathbf{V}_e = U_c \mathbf{e}_1 + \text{grad } \phi \quad (\text{IV-1})$$

where  $\phi$  is the velocity potential

$$\phi = -AU_c e^{-kz} \sin kx \quad (\text{IV-2})$$

( $x, z$ ) are cartesian coordinates with  $x$  positive downstream and  $z$  positive downwards (see figure 7), and  $\mathbf{e}_1$  is the unit vector in the  $x$ -direction. The third coordinate  $y$  is normal to the plate. The origin is located at the intersection of the plate leading edge and the undisturbed water level. The free-surface elevation  $\eta_e$  and the piezometric-pressure coefficient  $C_{p_e}$  are given to second order by

$$\eta_e(x) = - (1/2kA^2 + A\cos kx + 1/2kA^2\cos 2kx) \quad (IV-3)$$

$$Cp_e(x, z) = 2Ake^{-kz}\cos kx - (Ak)^2e^{-2kz} \quad (IV-4)$$

where  $Cp_e = P_e/(1/2\rho U_c^2)$  and  $P_e$  is the piezometric pressure. With regard to calculating the boundary layer on the plate, the most important quantities are the edge velocities

$$U_e/U_c = 1 - Ake^{-kz}\cos kx \quad (IV-5)$$

$$W_e/U_c = Ake^{-kz}\sin kx \quad (IV-6)$$

and the piezometric-pressure-gradient coefficients

$$P_x = \partial(P_e/\rho U_c^2)/\partial x = -Ak^2e^{-kz}\sin kx \quad (IV-7)$$

$$P_z = \partial(P_e/\rho U_c^2)/\partial z = -Ak^2e^{-kz}\cos kx + k(Ak)^2e^{-2kz} \quad (IV-8)$$

The dispersion relationship is

$$U_c^2 = g/k(1 + (Ak)^2) \quad (IV-9)$$

The second-order terms have been included since they have a significant influence for steep waves.

The wave elevation, edge velocities, and piezometric-pressure gradients are shown to first order in figure 8. Referring to figure 8, it is seen that four potential-flow regions can be distinguished. In region I, both  $P_z$  and  $P_x$  are favorable,  $W_e > 0$  and accelerating and  $u_e < U_c$  and accelerating, where  $u_e/U_c = U_e/U_c - 1$ . In region II,  $P_x$  is favorable and  $P_z$  is adverse,  $W_e > 0$  and decelerating and  $u_e > U_c$  and accelerating. In region III, both  $P_z$  and  $P_x$  are adverse,  $W_e < 0$  and decelerating and  $u_e > U_c$  and decelerating. In region IV,  $P_z$  is favorable and  $P_x$  is adverse,  $W_e < 0$  and accelerating and  $u_e < U_c$  and decelerating. Each of these regions has a distinct influence on the boundary-layer development.

## 2. Boundary Layer

The boundary-layer equations must be integrated numerically to obtain the velocity field for specified external-flow pressure gradients and edge velocities. The fully-implicit finite-difference method of Nash and Scruggs (1976), originally developed for aircraft applications, has been used. This method was improved by Patel et al. (1979, 1983, 1985) and applied to bodies of revolution at incidence and to ship forms for zero Froude number. Stern (1986) made some further modifications and applied the method to the Stokes-wave/flat-plate flow field and the Wigley hull for nonzero Froude numbers (Stern, 1985).

An overview of the method is as follows. The first-order boundary-layer equations are written in finite-difference form as

$$B_1 F_{m+1,n}^l + B_2 F_{m,n+1}^l + B_3 F_{m,n}^l + B_4 F_{m-1,n}^l + B_5 F_{m,n-1}^l = B_6 F_{m,n}^{l-1} - A_6 \quad (\text{IV-10})$$

where  $(l, m, n)$  are node-point indices in the  $(x, y, z)$  directions, respectively,  $B_{1-6}$  and  $A_6$  are coefficient matrices, and  $F = (U, W, \bar{q}^2)$ . The velocity components  $(U, W)$  are in the  $(x, z)$  Cartesian coordinate directions, and  $\bar{q}^2$  is the turbulence intensity, i.e., twice the turbulent kinetic energy. The turbulence intensity is determined from the Bradshaw/Nash one-equation wall-turbulence model with a simple modification to account for the free surface. In obtaining (IV-10),  $x$ -derivatives are expressed using backward differences, the first order  $y$ - and  $z$ -derivatives are expressed using upwind differencing so as to preserve convective stability, and lastly, second-order  $y$ -derivatives are expressed using a central difference.

The forward-marching procedure advances in the positive  $x$ -direction from a cross-plane  $l-1$ , where the solution is assumed to be known, to a cross-plane  $l$ , at which a new solution is obtained by solving equation (IV-10) using an ADI scheme. After each  $n$ - or  $m$ -scan, the continuity equation is integrated to obtain the  $V$ -velocity component, which is in the  $y$ -direction. The coefficient matrices are updated in successive iterations until convergence is obtained with respect to the velocity components at each grid point within a specified tolerance.

The thickness of the integration domain is  $1.26\delta(x, z)$ , where  $\delta$  is the boundary-layer thickness. Note that  $\delta$  is determined as part of the solution. The number of grid points is kept constant in the  $y$ - and  $z$ -directions. Expanding grids are used in these directions in order to resolve the flow near the wall and the free surface, respectively. The step size  $\Delta x$  is arbitrarily specified. The usual boundary conditions are used, except at the free surface where a symmetry-condition approximation to the free-surface boundary conditions is applied.

## B. Calculation Conditions

The conditions for the calculations were specified in order to simulate those of the experiments. Calculations were performed for carriage speed  $U_c = 1.37\text{m/s}$  and two values of wave steepness  $Ak = (.11, .21)$ . Based on these, the wave length  $\lambda$  is 1.19 and 1.15m, respectively, according to equation (IV-9); however, here we simply assume the linear-theory value  $\lambda \sim 1.2\text{m}$ . Thus,  $Re_\lambda = 1.64 \times 10^6 (= U_c \lambda / \nu)$ , assuming an average water temperature of  $20^\circ\text{C}$ . Transition was specified at  $x/\lambda = .05$ , which corresponds to the location of the trip studs in the experiments. 170  $x$ -steps and 21 grid points across the boundary layer were used. In the  $z$  direction, 8 grid points were used, i.e.,  $z/\lambda = (0., .025, .0619, .1164, .1969, .3156, .4911, .75)$ . Since, in general, the calculation and experimental locations did not coincide, the calculations were interpolated onto the experimental locations using piecewise Hermite splines.

# V. EXPERIMENTAL AND THEORETICAL RESULTS

## A. Wave Profiles

First the wave profiles were measured to determine the wavemaking characteristics of the horizontal-submerged foil. Of present interest is the ability to generate waves with properties similar to Stokes waves and to control both the wave steepness  $Ak$  and the wavelength  $\lambda$  by adjustment of the foil submergence  $d$  and the carriage speed  $U_c$ . The experiments of Salvesen (1966) and Salvesen and von Kerczek (1975), which were described in Section III.A, indicated that this would be possible with the present arrangement; however, the influence of the downstream plate was not known. Wave profiles were

recorded photographically for  $d/c = (.96, .99, 1.12, 1.24, 1.39)$  and for  $U_c$  ranging from .91 to 1.68m/s. Figure 9 shows the wave profile for  $d/c = 1.12$  and  $U_c = 1.37\text{m/s}$ , and is representative of the other results obtained. As will be shown subsequently through detailed comparisons, the wave profile  $\eta_e$  and velocity field  $V_e$  (velocity field external to the plate boundary layer) are, in fact, similar to a second-order Stokes wave; however, there are some differences. In particular, the plate has a damping influence such that the second wave crest  $\eta_2$  is smaller than the first  $\eta_1$ . Referring to figure 9, the damping factor

$$\mu = \ln(\eta_1/\eta_2) \quad (V-1)$$

is  $\mu = .34$ . Typically,  $.25 < \mu < .6$ . Note that in Salvesen's experiments  $\mu \sim 0$ . The wave steepness  $Ak$  was determined from the measured average (first two crests and included trough) wave height  $H$  and wavelength  $\lambda$  as

$$Ak = H\pi/\lambda \quad (V-2)$$

where  $H$  is measured from crest to trough. The wavelengths  $\lambda$  were generally shorter than those from linear theory; however,  $\lambda$  was difficult to determine accurately from the photographs and in some cases was estimated from linear theory, i.e.

$$\lambda = 2\pi U_c^2/g \quad (V-3)$$

(cf. equation (IV-9)).

The results for  $Ak$  vs.  $U_c$  for each  $d/c$  investigated are shown in figure 10. As expected,  $Ak$  increases with decreasing  $d/c$ . Also,  $Ak$  is maximum for a certain  $U_c = U_{\max}$ , which appears to decrease somewhat with  $d/c$ . For  $d/c = 1.39$ ,  $U_{\max} = 1.4\text{m/s}$ , whereas for  $d/c = 1.12$ ,  $U_{\max} = 1.3\text{m/s}$ . For  $d/c < 1.12$ , a wave-breaking phenomenon occurred for large  $Ak$ , i.e., for  $Ak > Ak_{\max} \sim .31$  a highly disturbed region with the appearance of a hydraulic jump was observed at the free surface originating just upstream of the first wave crest. The disturbance usually initiated at the end plates and then propagated across the width of the tank. Similar disturbances were reported by

Salvesen (1966) and others. Further discussion of this phenomenon, including its similarities and relevance to wave-induced separation, is provided in Chapter VI. Wave-steepness values determined from the wave profiles presented by Salvesen (1966) and Salvesen and von Kerczek (1975) are also shown on figure 10. Consistent with the previous discussion concerning the damping influence of the plate, their wave-steepness values are larger than the present ones for similar values of  $d/c$ . Salvesen and von Kerczek (1975) estimate  $Ak_{\max} \sim .35$ .

The results from the wave-profile measurements confirm that the wave system of the foil-plate model has properties similar to Stokes waves; however, the plate has a damping influence. The damping influence and other differences will be discussed more fully in Section V.C with regard to the velocity measurements. Also, the results for the wave steepness indicate that for  $1.2 < U_c < 1.7 \text{ m/s}$   $Ak$  varies considerably as a function of  $d/c$ . This was helpful in the selection of conditions for the velocity measurements.

#### **B. Wave-Induced Separation**

Very little is known about wave-induced separation, i.e., three-dimensional boundary-layer separation near the free surface induced by waves and accompanied by a large disturbance to the free surface itself. It was first identified and demonstrated experimentally by Chow (1967) with two-dimensional struts mounted vertically and piercing the free surface in a hydraulic flume. The struts were designed for unseparated flow when no waves are present, i.e., at large depths. For a foil strut, Chow observed regions of separated flow originating just beyond the wave trough and extending up to and in some cases beyond the trailing edge. The depth of the separated-flow region was of the order of the wave height and the length was shown to depend on the Froude number. Chow observed streamwise flow reversal as well as large cross flow within the separated-flow region. Calculations of the separation starting point using Stratford's laminar-separation criterion were shown to be in agreement with the observations.

Wave-induced separation is also exhibited in the present experiment. Although barely visible in figure 9, a close-up photograph of the separation region for the same conditions as figure 9 is shown in figure 11a, which

clearly displays the phenomenon. An even more detailed view is shown in figure 11b, which is for conditions producing a larger and more disturbed separation region ( $d/c = .96$ ,  $U_c = 1.6\text{m/s}$ ). A schematic view of the separation region is shown in figure 12. Based on the present experimental results, the following general features of wave-induced separation can be identified:

- (a) wedge-shaped region;
- (b) unsteady turbulent (highly disturbed and broken) free surface;
- (c) separation region is demarcated by a wave front across which the free-surface slope is discontinuous;
- (d) interaction region between wave induced-separation and waves generated by the displacement effects of the upstream boundary layer;
- (e) depthwise extent is on the order of the wave height; and
- (f) occurrence coincides with an adverse streamwise piezometric-pressure gradient and vertical velocities towards the free surface.

For most conditions, the wave-front angle  $\beta$  (see figure 12) appears to be about  $20^\circ$ , but was difficult to determine accurately from the photographs. However, it was possible to estimate the variation of the separation starting point  $x_s$  vs.  $Ak$ , as shown in figure 13. In figure 13,  $x_s$  is normalized with respect to the wavelength, i.e.

$$L_s = (x_s - x_{\eta_1})/\lambda \quad (V-4)$$

where  $x_{\eta_1}$  is the  $x$ -coordinate at the first wave crest  $\eta_1$ . Results are shown for  $d/c = (.96, .99, 1.12)$ . It was anticipated that Reynolds number effects would be weak such that the results for each  $d/c$  would coincide. Although true for  $d/c = (.96, .99)$ , the results for  $d/c = 1.12$  indicate smaller values of  $L_s$ , i.e., larger separation regions. Also shown on figure 13, next to each data point are the associated values of  $\lambda$  and Reynolds number based on  $x_s$ , i.e.,  $Re_{x_s} = U_c x_s / \nu$ . It is seen that for  $d/c = 1.12$ , generally,  $\lambda$  and  $Re_{x_s}$  are smaller than they are for  $d/c = (.96, .99)$ .

Although we were able to observe certain features of wave-induced separation, it was not possible to determine the nature of the flow within the separation region. For this purpose, some flow-visualization studies were conducted using a hypodermic needle with colored dye, but due to the small



depthwise extent of the region and highly disturbed free surface it was difficult to reach conclusions. Large-scale streamwise flow reversal was not evident, suggesting, at least for the present circumstances, an open- as opposed to a closed-type separation. Velocity measurements to determine the flow pattern are desirable; however, a large portion of the separation region is above the undisturbed water level which makes yaw-probe measurements difficult and none were made.

The previous Stokes-wave/flat-plate calculations (Stern, 1986) also indicated the occurrence of wave-induced separation. Separation was deemed to occur when the streamwise shear-stress component became  $\leq 0$ . In the laminar-flow calculations ( $Re_\lambda = 2 \times 10^4$ ), which were performed for  $Ak = (.01, .1, .2, .3)$ , this occurred for all but the lowest  $Ak$  value. In the turbulent-flow calculations ( $Re_\lambda = 5 \times 10^6$ ), which were performed for  $Ak = (.01, .1, .2, .3, .35)$ , this only occurred for the highest  $Ak$  value. The predicted separation starting point from these calculations and from Stratford's laminar-separation criterion are also shown on figure 13. For laminar flow, as would be expected, large separation regions are predicted (i.e., small  $L_s$ ), even for the lower  $Ak$  values. Note that the laminar-flow calculations and Stratford's laminar-separation criterion are in fairly good agreement, although the latter indicates smaller values by about 10%. For turbulent flow, the predicted separation starting point is considerably larger than that that would be expected from the experiments for  $Ak = .35$ . The present calculations (see Section IV.B) are for turbulent flow and  $Ak = (.11, .21)$ ; thus, separation did not occur. Recall that the present results as well as the previous ones just referred to were obtained through the use of the usual first-order boundary-layer equations with a symmetry-condition approximation to the free-surface boundary conditions. As discussed previously, such an approach is not valid in the region very near the free surface. In this region, even without the occurrence of wave-induced separation, the free-surface boundary conditions play an important role and higher-order equations are required. It is evident that more advanced computational fluid dynamics techniques than those used presently are required to predict the flow very near the free surface, including wave-induced separation. In such a computational study, a critical issue that needs to be resolved is the determination of appropriate free-surface boundary conditions for turbulent flow, especially for conditions under which

wave-induced separation occurs. To aid in our understanding of wave-induced separation, some relevant free-surface phenomena which appear to have common features are discussed in Chapter VI.

### C. Velocity Profiles

Conditions for the velocity-profile measurements were selected based on the results of the wave-profile measurements. It was desired to have the wavelength large so that the boundary layer would be thick, and also, for a fixed wavelength, to have a sufficient variation in  $Ak$  as a function of  $d/c$  to enable measurements for both large- and medium-steepness conditions. Note that the former requires large  $U_c$  (see equation (IV-9) or (V-3)). Referring to figure 10, the conditions selected are:

$$\begin{aligned} \text{large steepness: } U_c &= 1.37\text{m/s, } d/c = 1.12, \\ \text{medium steepness: } U_c &= 1.37\text{m/s, } d/c = 1.39. \end{aligned} \quad (V-5)$$

For both conditions the wavelength  $\lambda \sim 120\text{cm}$ , so that  $Re_\lambda = 1.64 \times 10^6$  ( $= U_c \lambda / \nu$ ), assuming an average water temperature of  $20^\circ\text{C}$ . Referring to figure 7, measurements were made for up to four depths  $z/\lambda = (.04, .08, .125, .25)$  and eight axial locations  $x/\lambda = (.125, .25, .375, .5, .625, .75, .875, 1)$ . Note that  $(x, z) = (0, 0)$  is at the intersection of the plate leading edge and the undisturbed water level. To aid in ascertaining the effects of the waves on the boundary-layer development, an additional set of measurements were made for conditions which simulate zero-steepness, i.e., a flat free surface.

In the following, the zero-steepness results will be discussed first and then the large- and medium-steepness conditions. For each condition, experimental results are shown for the edge-velocity ( $U_e, W_e$ ) and piezometric-pressure  $C_p$  distributions, streamwise  $U$  and cross-flow  $W$  velocity profiles, streamwise displacement thickness  $\delta^*$ , magnitude of the wall-shear stress  $C_f$ , and other quantities of interest. Also, comparisons are made with the theoretical values. The experimental edge velocities were determined by fitting least-square splines to the data. All integral parameters ( $\delta^*$ , etc.) were determined by trapezoidal-rule integration. The accuracy of the integration is not as good for the experimental profiles as it is for the calculated ones due to the smaller number of data points obtained for the former. The experi-

mental values for  $C_f$  were determined from a Clauser chart. In the figures, the experimental values are shown by symbols, and the calculated values by solid curves. In the velocity-profile figures, the outermost point is at 1.26 $\delta$  where the velocity components have their edge values. This point was a boundary condition in the calculations, but, in general, not a measurement point. In the presentation of the results and the discussions to follow, all variables, unless otherwise indicated, are nondimensionalized using the wavelength  $\lambda$ , carriage velocity  $U_c$ , and fluid density  $\rho$ . In most of the discussions, attention is first focused on the experimental results and then these are compared with the theoretical values.

### 1. Zero Steepness

In order to simulate conditions corresponding to zero steepness measurements were made both with the foil deeply submerged (i.e.,  $d/c = 2.75$ ) and with the foil removed. Although in both cases the wave effects are small ( $2A \sim 2\text{cm}$ ,  $\lambda \sim 120\text{cm}$ ,  $Ak \sim .05$ ), they are actually less for the foil installed and  $d/c = 2.75$  than for the foil removed. Apparently, for the former condition, the plate- and foil-induced waves cancel resulting in a flatter free surface. Only the results for the foil deeply submerged will be presented.

As indicated above, the primary purpose of the zero-steepness measurements is for comparison with the large- and medium-steepness conditions. It is also of interest to evaluate the differences between the present flow and the benchmark results for two-dimensional flat plate turbulent boundary layers due to the present nonideal conditions, i.e., free-surface effects and relatively low Reynolds number.

For  $U_c = 1.37\text{m/s}$  and  $d/c = 2.75$ , velocity measurements were made for  $z = .08$  and  $x = (.25, .5, .75, 1)$ . The results are shown in figure 14, including the corresponding calculations (i.e., the computed results at the greatest depth  $z = .75$ , where the flow is essentially two-dimensional) for comparison. The experimental results for the U-velocity component show the expected features of a two-dimensional flat-plate turbulent boundary layer, except for  $x = .25$  where large differences are seen both in the edge value and the shape of the velocity profile. The differences in edge values are attributable to free-surface effects. In particular, the plate induces a small-amplitude

leading-edge wave (see figure 7) such that the streamwise velocity component is reduced near the plate leading edge (crest region). As to the differences in shape, it appears that the plastic studs at  $x = .05$  are not completely effective such that at  $x = .25$  the flow is in transition and not fully turbulent. Of course, the W-velocity component is zero for two-dimensional flow, however, in the experiments there is a small W component ( $W/U_c < 2.5\%$ ). Here again, this is attributed to free-surface effects. Note that the experimental edge values and cross flow are consistent with the  $d/c = 2.75$  wave profile (see figure 7). The comparison between the calculations and the measurements is quite good, except for  $x = .25$  for the reasons noted above. The experimental boundary-layer thickness is about 10% thicker than the calculated one. Also shown in figure 14 are the calculated turbulence-intensity profiles  $q^{-2}$ , although no experimental data were obtained for comparison.

Figure 15 shows a comparison of the wall-shear-stress magnitude  $C_f$  obtained from the measurements based on the Clauser chart, the calculations, and the benchmark momentum-integral analysis presented by White (1974). The latter, according to White, is within 5% of all the data for smooth plates. The abscissa is  $Re_\delta^* (= U_c \delta^* / \nu)$  rather than  $x$  or  $Re_x$  so that  $C_f$  should be independent of the transition point. Generally, the experimental values are smaller than the benchmark values and show a larger slope. These differences are due both to the present nonideal conditions and the use of the Clauser chart. The values of the constants in the logarithmic-overlap law used in generating the Clauser chart may not be the same as those that would be consistent with the present experimental data. The calculations are about 10% below the benchmark values and have the same slope.

Figure 16 shows a similar comparison for the shape parameter  $H = \delta^* / \theta$ , where  $\theta$  is the momentum thickness. The experimental values are larger than the benchmark values, but converge towards them (at  $x = 1$ , the difference is about 15%). In the laminar-flow region, the calculated  $H$  is about 1% below the Blasius value. In the turbulent-flow region, the trend of the calculations is similar to that of the experiments, but with smaller values (at  $x = 1$ , the difference from the benchmark values is about 5%).

The velocity profiles are plotted using inner- and outer-law variables (see List of Symbols for definitions) in figures 17 and 18, respectively.

Also shown on figure 17, are the linear-sublayer and logarithmic-overlap laws. In the latter case, the values of the constants used were  $\kappa = .4$  and  $B = 5.5$ . Also shown on figure 18, is the theoretical zero-pressure-gradient equilibrium wake profile of Mellor and Gibson (1966). Referring to figure 17, it is seen that the experimental profiles, with the exception of  $x = .25$ , show the expected behavior in the logarithmic-overlap and outer regions, although there are only about three experimental data points in the former and the one closest to the wall is in error due to interference effects between the probe and wall. The slope of the logarithmic portion is consistent with  $\kappa = .4$ , but the additive constant is larger  $B \sim 6$ . In the outer region, the profile shapes and distances above the logarithmic-overlap law are consistent with Coles wake function. Again, the calculations and experiments are in agreement, except for  $x = .25$ . Besides the logarithmic-overlap and outer regions, the calculations are also seen to represent well the sublayer and blending zones. Referring to figure 18, it is seen that, with the exception of the experimental profile for  $x = .25$ , the profiles are in reasonable agreement with the theory.

It is concluded that, for conditions which simulate zero steepness (i.e., the foil deeply submerged), the boundary-layer development on the plate shows the typical characteristics of a two-dimensional flat-plate turbulent boundary layer; however, there are some differences, especially near the leading edge, which are attributable to free-surface and low-Reynolds-number effects. The agreement between the measurements and the calculations is generally quite good, and both agree well with the benchmark results.

## 2. Large Steepness

The wave profile shown in figure 9 corresponds to the large-steepness condition; however, for the velocity-profile measurements, the longitudinal position of the plate was adjusted so that the plate leading edge coincided with the first wave crest (see figure 7). Figure 19 is a photograph of the flow near the leading edge. Superimposed on the free surface of the Stokes wave is a small-amplitude short-wave-length diverging-wave system, which is due to leading-edge effects associated with the finite-thickness of the plate and the plastic studs at  $x = 6\text{cm}$  used to induce turbulent flow. Recall, as we have already pointed out, the occurrence of a plate-induced leading-edge wave (i.e., a transverse wave system). Hereafter, all such effects will be refer-

red to as leading-edge effects of the plate. Figure 11a is a photograph of the flow near  $x = \lambda \sim 120\text{cm}$ , which shows the wave-induced separation for the present condition.

Measurements were made for  $z = (.04, .08, .125)$  and  $x = (.125, .25, .375, .5, .625, .75, .875, 1)$  and also for  $z = .25$  and  $x = (.25, .5, .75, 1)$ ; however, only the former are presented. The results for  $z = .25$  suffered from the wake of the upstream foil and inaccuracies due to calibration difficulties at this large depth, as discussed in Section III.C. Results for  $z = .25$  are included for the medium-steepness condition where the foil-wake effects are less severe.

The measured edge-velocity distribution is shown in figure 20. The measurements show the typical characteristics of a two-dimensional wave, i.e.:  $U_e$  is minimum at the crests  $x = (0,1)$ , close to 1 at the nodes  $x = (.25, .75)$ , and maximum at the trough  $x = .5$ ;  $W_e$  is close to zero at the crests and trough, and maximum and minimum at the first and second nodes, respectively. Note that the wave is aperiodic since the first crest is somewhat larger than the second. As discussed above, this is due to the leading-edge effects and damping influence of the plate.

Also shown on figure 20 are the second-order Stokes-wave values for  $Ak = .21$ . This value of  $Ak$  was selected to give the best overall agreement between theory and experiment. In general, the experimental and theoretical values are both qualitatively and quantitatively in close agreement which confirms that the differences between the wave system of the foil-plate model and a Stokes wave are relatively small. To display further the nature of the differences, a comparison is shown in figure 21 between the experimental and theoretical piezometric-pressure distribution. The experimental values were obtained from the measured edge velocities through the use of the Bernoulli equation. Also shown on figure 21 are both the measured wave profile and the second-order Stokes-wave elevation. As expected, the level of agreement between the experimental and theoretical values of  $C_p$  is similar to that shown for the edge velocities. The measured wave profile and edge pressure are in most cases consistent, i.e., the maximum and minimum values of  $C_p$  are at the free surface. The largest discrepancies between the measured wave profile and the second-order Stokes-wave elevation are at the ends. For  $x <$

.25, the experimental wave elevation is larger than the theoretical one, due to the leading-edge effects of the plate. For  $x > .75$ , the experimental wave elevation is smaller than the theoretical one due to the damping influence of the plate. In the mid region ( $.25 < x < .75$ ), the agreement is rather good. The inconsistencies between the theoretical wave elevation and piezometric-pressure distribution for  $.25 < x < .75$  are due to the fact that the latter was evaluated along lines of constant  $z$  and not streamlines. It should be recognized that the Stokes-wave velocity and piezometric-pressure distributions shown in figures 20 and 21, respectively, are the edge values prescribed in performing the boundary-layer calculations for the large-steepness condition.

The detailed velocity profiles, both measured and calculated, are shown in figures 22a-c for all  $x$  values and  $z = (.04, .08, .125)$ , respectively. Referring to figure 22a, with regard to the  $U$ -velocity component, it is seen that initially, at  $x = .125$ , the profile appears laminar, at  $x = .25$  the profile is transitional, and for  $x > .25$  the profiles are turbulent. The low- $Re$  effects near the leading edge  $x = (.125, .25)$  were noted and discussed previously in the zero-steepness results (see Section V.C.1). With regard to the  $W$ -velocity component, the outer part of the profile is relatively flat, but the inner part shows dramatic changes over the wavelength. The effects of the variations of the external-flow piezometric-pressure gradients on the boundary-layer development, which were discussed previously in explicating the calculations (Stern, 1986), are also clearly visible in the measurements. In particular, in response to  $P_x$ , the  $U$ -velocity component is accelerating for  $x = (.125, .25, .375, .5)$  and the boundary-layer-growth rate is small; but it is decelerating for  $x = (.625, .75, .875, 1)$  and the boundary-layer-growth rate is large. At this depth, the boundary layer is thick for  $x = (.125, .25)$ , such that the acceleration actually thins the boundary layer, i.e., the boundary layer thickness at  $x = .375$  is less than that at  $x = .25$ . In response to  $P_z$ , the  $W$ -velocity component shows alternating direction. First, for  $x = (.125, .25)$ ,  $W$  is positive and increasing. Subsequently, beginning with the inner part of the profile first,  $W$  becomes negative ( $x = .375, .5, .625, .75$ ). Lastly, for  $x = (.875, 1.)$ , again beginning with the inner part of the profile first,  $W$  becomes positive. It is remarkable how the inner part of the  $W$ -velocity component responds first to the changes in the external flow.

Referring to figures 22b,c, the results at greater depths show very similar trends to those just discussed, but with reduced amplitudes in their deviation from two-dimensional flow due to the decay of the external-flow piezometric-pressure gradients. Also, the boundary-layer thickness at  $x = (.125, .25)$  is not as large as it is for  $z = .04$ .

Generally, close agreement is shown between the calculations and the measurements both for the thickness of the boundary layer and the shape of the profiles, except near the leading edge. For  $x = (.125, .25)$ , along with the above discussed differences in edge values, differences are also seen across the boundary layer. The experimental boundary-layer thickness is considerably larger than the calculated one and the shape of the profiles, especially the U-velocity component, is quite different. The calculations display typical turbulent-flow characteristics, whereas as just discussed, the experimental flow shows low-Re effects. The calculated W-velocity component shows a more gradual variation across the boundary layer than the experiments. For  $x > .25$ , as already noted the agreement is very good. The differences in the U-velocity profile are primarily due to the differences in edge values. It is noteworthy how accurately the W-velocity component is predicted. The experiments indicate a somewhat faster depthwise decay rate than the exponential decay rate specified in the calculations. Also shown on figure 22 are the calculated turbulence-intensity profiles  $\bar{q}^2$ . A comparison of the  $\bar{q}^2$  profiles in figure 22a with those shown for two-dimensional flow in figure 14 indicates that, during the acceleration phase, the maximum value is increased and occurs closer to the wall. Subsequently, during the deceleration phase, the maximum value is reduced and occurs more towards the middle of the boundary layer.

The measured streamwise displacement thickness  $\delta^*$  is shown in figure 23. Also shown are the values from the zero-steepness experiments and the calculations for comparison. Initially, for  $x = .125$ , the measured displacement thickness at  $z = .04$  is considerably larger than that at the greater depths. This is consistent with the boundary-layer thickness trends shown in figure 22. For  $x = .25$ , the displacement thicknesses for all three depths have about the same value which is close to that for zero steepness. Subsequently, for  $x = (.375, .5)$ , the results for large steepness clearly show a reduction in displacement thickness as compared with the zero-steepness condition. Although the greatest reduction is for  $z = .04$ , the values for all



three depths are similar. Note that the rate of reduction is largest for  $x = .375$ . Finally, for  $x = (.625, .75, .875, 1)$ , the trend is reversed; i.e., the results for large steepness show increased values as compared with those for zero steepness. In this case, the variation with depth is quite evident with the largest increases occurring for decreasing depth. Note that the rate of increase is largest for  $x = .875$ . The trends just described are a direct result of the influences of the external-flow piezometric-pressure gradients, including the strong influence of the three-dimensionality of the flow; i.e., the fact that the largest rates of decrease and increase occur for  $x < .5$  and  $1$ , respectively, is due to the influence of  $P_z$ . The minimum and maximum values show a 39% and 30% change from the zero-steepness values, respectively.

Here again, generally, close agreement is shown between the calculations and the measurements. The  $z = .75$  solution and the zero-steepness measurements show very similar values, although for  $x = 1$  the measured value is somewhat larger than the calculated one. For the large-steepness condition and  $z = .04$ , the measurements and calculations are in close agreement except at the ends where the differences are seen to be consistent with the previous discussions. For  $z = (.08, .125)$ , both the calculations and measurements indicate similar trends, although the calculations exhibit a larger variation with depth than the measurements. The maximum and minimum values show about a 33% and a 76% change from the deep solution, respectively. It is noteworthy that the magnitude of the free-surface effects on the displacement thickness both measured and predicted are substantially in agreement.

Figure 24 shows a similar comparison for the wall-shear-stress magnitude  $C_f$ . The experimental values were obtained through the use of the Clauser chart. It is seen that the wall-shear-stress behavior is consistent with the previously described displacement thickness, but in reverse trend. Note that the shear stress responds more quickly, and with greater intensity to changes in the external flow than the displacement thickness. Initially, for  $x = .125$ , the wall-shear stress at  $z = .04$  is considerably smaller than that at the greater depths. For  $x = .25$ , the wall-shear stress for all three depths have similar values which are somewhat larger than that for zero steepness. Subsequently, for  $x = (.375, .5)$ , the results for large steepness show a large increase over the zero-steepness values. The shallower the depth the larger the increase. The greatest increase occurs for  $x = .375$ . Finally, for  $x =$

(.625, .75, .875, 1), the trend reverses, i.e., the results for large steepness show smaller values than those for zero steepness. The shallower the depth the larger the reduction. Note that the largest reduction occurs for  $x = .875$ . The maximum and minimum values show a 62% and 33% change from the zero-steepness values, respectively.

As has been the case throughout, generally, close agreement is shown between the calculations and the measurements. The  $z = .75$  solution was previously compared with the zero-steepness measurements in figure 15 in which the abscissa is  $Re_\delta^*$  instead of  $x$ , as it is in figure 24. The trends shown in both figures are identical, although they are less exaggerated when  $x$  is used for the abscissa. For the large-steepness condition the comparison is quite good, although the calculations indicate a larger increase and decrease than the experiments. The maximum and minimum values show about a 76% and a 68% change from the deep solution, respectively.

### 3. Medium Steepness

The wave profile corresponding to the medium-steepness condition is shown in figure 7. Here again, the longitudinal position of the plate was adjusted so that the plate leading edge coincided with the first wave crest. Similar leading-edge free-surface effects were present for this condition as those described previously for the large-steepness condition. Although the free surface near  $x = \lambda$  was somewhat disturbed, no wave-induced separation occurred. Measurements were made for  $z = (.04, .08)$  and  $x = (.125, .25, .375, .5, .625, .75, .875, 1)$  and for  $z = (.125, .25)$  and  $x = (.25, .5, .75, 1)$ .

The results are shown in figures 25 through 29 in which the same format has been used as that for the large-steepness condition. Figure 25 shows the edge velocities. Figure 26 shows the piezometric-pressure distribution. Figure 27 shows the velocity and turbulence-intensity profiles. Lastly, figures 28 and 29 show the streamwise displacement thickness and the magnitude of the wall-shear stress, respectively.

As discussed previously with regard to the large-steepness condition, the wave steepness is selected to give the best overall agreement between theory and experiment for the edge-velocity distribution. Referring to figure 25, for the present condition,  $Ak = .11$  was used. In general, the present experimental trends are consistent with the large-steepness condition, except with

reduced deviations from the zero-steepness values due to the smaller  $Ak$ ; however, the data are somewhat more irregular than that shown previously. As was the case for large steepness, the experimental and theoretical values are in close agreement.

## VI. SOME FREE-SURFACE PHENOMENA RELEVANT TO WAVE INDUCED SEPARATION

Wave-induced separation was discussed in Section V.B. To aid in our understanding of this phenomenon, some relevant free-surface phenomena which appear to have common features with the former will now be discussed.

The first is the small  $d/c$  wave-breaking phenomenon referred to in Section V.A which has been the subject of some recent investigations. Battjes and Sakai (1981) performed experiments with a NACA 6024 profile in a wave-current flume for  $d/c = 1$ , angle of attack  $= 15^\circ$ , and free-stream velocity  $U_0 = 1.08\text{m/s}$ . These conditions generate a wave with  $Ak \sim .34$  and an extensive region of wave breaking. They believe this flow to be similar to the later stages of a shallow-water spilling breaker. Their primary objective was to quantify the observations of Peregrine and Svendsen (1978) for quasi-steady hydraulic jumps, bores, and spilling breakers that the turbulent flow, immediately following breaking, resembles a turbulent-mixing layer. This appears to have been accomplished through laser-doppler-velocimeter measurements which show that the turbulent-flow field downstream of the initiation of the separation at the free surface resembles that in a self-similar turbulent wake with regard to the mean-velocity defect, turbulence intensity, and shear-layer thickness. Also, the gross features of the flow are shown to obey Froude scaling. However, these results must be viewed with some caution since the accuracy of the measurements is questionable. Although the depthwise extent of the measurements includes the foil wake, it is barely discernible.

Duncan (1983) performed experiments with a NACA 0012 profile in a 24m long and 61cm wide and deep tank for angles of attack of  $5^\circ$  and  $10^\circ$ ,  $U_0 = (.6, 1\text{m/s})$ , and variable  $d/c$ . Wave profiles and vertical distributions of mean velocity and total head were measured. The purpose of the study was to determine a breaking criterion and the contribution of breaking resistance to the total. For  $Ak \sim .31$ , breaking could be induced by dragging a light cloth on the water surface just upstream of the foil. For  $.31 < Ak < .35$ , the breaking

was spontaneous. Thus, Duncan concludes that the breaking criterion is  $Ak_{\max} = .31$ , which is consistent with the present results. The wake-survey measurements indicate that, under breaking conditions, the total drag is more than three times the potential-flow wave drag.

Mori (1986) performed experiments with a NACA 0012 profile in a circulating-water channel for an angle of attack of  $2^\circ$  and variable  $d/c$  and  $U_0$ . Wave profiles and vertical distributions of mean velocities and Reynolds stresses were measured. The latter quantities were obtained with an X-type hot-film probe. Breaking was observed for  $Ak_{\max} \sim .31$  which is consistent with the above discussions. Large velocity defects and turbulence intensities were shown near the free surface just downstream of the breaking-wave front. Breaking criteria were developed for some simple cases (linear and constant-curvature free surface) based on inviscid-flow instability analysis.

In summary, waves of sufficient steepness ( $Ak_{\max} \sim .31$ ) generated by a horizontal-submerged foil break and form a turbulent separation region near the free surface originating on the forward face of the wave where the stream-wise piezometric-pressure gradient is adverse and the vertical velocity is towards the free surface. The occurrence of flow reversal in the separation region and the size of the separation region depend on the intensity of the disturbance. The separation region mixes with the main flow in the same manner as a turbulent wake.

A considerable amount of work has been done, for the most part using inviscid-flow analysis, concerning the instability of deep-water waves (e.g., the review article of Yuen and Lake (1980)). Longuet-Higgins (1978) identifies two distinct types of instability: low wave-steepness instabilities with low rates of growth; and high wave-steepness local instabilities leading directly to wave breaking. Here we are concerned with the latter. The instability analysis of Longuet-Higgins (1978) indicates  $Ak_{\max} = .44$ . Similar values have been given by others, including Stokes (1880) using an argument locally valid near the crest to demonstrate that the limiting wave profile has a  $120^\circ$  corner at its crest, which is a stagnation point. Longuet-Higgins and Cokelet (1978) verify the instability analysis through numerical simulations of the exact nonlinear, unsteady, inviscid, spatially-periodic wave problem. It is apparent that the results from inviscid-flow analysis are not in accord

with the experimental results for waves generated by horizontal-submerged foils. To our knowledge they have not been confirmed by experiments for waves generated by other configurations either. Thus, one cannot be certain that all the physical mechanisms responsible for breaking and free-surface separation are well represented by inviscid-flow theory. Although the gross features of the flow obey Froude scaling, the fact that breaking and free-surface separation can be triggered by sidewall boundary layers and free-surface shear indicates the importance of nonuniformities and, no doubt, viscosity.

Next we discuss the complex, nonlinear, nondispersive free-surface phenomena exhibited in the near field of ships. Baba (1969) first identified the importance of such phenomena, i.e., breaking bow waves and their large contribution to resistance. Subsequent investigations, most notably the extensive program of towing-tank experiments at the University of Tokyo (Inui, 1981), have demonstrated in more detail, not only breaking bow waves, but the occurrence of a separation zone and vortices ahead of the bow and other breaking waves originating both along the forebody shoulder and in the stern region. For a variety of ship and wedge models, the near-field wave patterns were studied using overhead photography, often with an aluminum powder film on the water surface to enhance flow visualization, along with some wave-height and mean-velocity and pressure-field measurements. For purposes of discussion, these experiments are conveniently divided into those pertaining to the forebody and the afterbody.

Miyata and Inui (1984) have summarized the work concerning the waves originating on the forebody (bow and shoulder). The following typical characteristics of the near-field waves, which they refer to as free-surface shock waves, are identified:

- (a) the wave patterns are due to nonlinear and viscous effects and are not part of Kelvin's linear dispersive wave system;
- (b) they originate in regions with large-wave steepness;
- (c) the appearance of the free surface is unsteady and turbulent on and behind the wave fronts;
- (d) the region in which the flow undergoes an abrupt change in velocity is limited to a thin layer near the free surface;
- (e) the wave-crest-line angle varies with the Froude number and ship-model geometry;

- (f) the velocity magnitude drops rather suddenly at the wave front in such a manner that the component normal to the wave-front line is considerably decreased, whereas the tangential component is almost conserved;
- (g) dissipation of wave energy into momentum loss far behind the ship models occurs; and
- (h) the gross features of the flow obey Froude scaling.

Doi (1980), Doi et al. (1981, 1982), and Doi and Kajitani (1986) report on the work concerning the characteristics of near-field stern waves. The principal results from this work are as follows:

- (a) the characteristics of stern waves are similar to those of forebody waves;
- (b) their starting point is Froude-number dependent and occurs in regions of large-wave steepness and upward oriented flow;
- (c) the wave-front angle ( $10^\circ < \beta < 40^\circ$ ) is strongly dependent on body geometry and weakly dependent on Froude number;
- (d) a large velocity defect occurs near the free surface downstream of the wave front;
- (e) gross features obey Froude scaling, however, free-surface turbulence intensity does not;
- (f) wave resistance shows significant increase for conditions leading to large stern waves (i.e., separation position moves forward and  $\beta$  large), which are dependent on body geometry and Froude number; and
- (g) stern waves can be controlled by attenuating the wave slope or suppressing the upward oriented flow.

Although the wave-induced separation exhibited in the present experiment is, no doubt, most closely related to the just described near-field stern waves, it appears that both of these have certain features in common with the previous descriptions of both the near-field forebody waves and the small d/c wave-breaking/free-surface-separation phenomenon. In particular, all four appear to have the following in common:

- (a) unsteady turbulent (highly disturbed and broken) free-surface separation region;

- (b) separation zones originate in regions of large-wave steepness where the streamwise piezometric-pressure gradient is adverse and the vertical velocity is towards the free surface;
- (c) the separation region is demarcated by a wave front across which the free-surface slope is discontinuous;
- (d) depthwise extent is on the order of the wave height; and
- (e) the separation region is a velocity-defect region which mixes with the main flow downstream in the same manner as a turbulent wake.

Of course, there are differences between the free wave and body-generated wave situations due to the interactions with the body boundary layer and wake in the latter case, especially near the stern. We have tried to identify common features in order to aid in our understanding of these complex flow phenomena.

In spite of the engineering importance of such phenomena, especially for ship design, at present only a qualitative understanding exists. In fact, the interpretation of these flow structures can be quite different. As discussed by Inui (1981), some consider the above a wave-breaking type phenomena and thus closely related to the dispersive wave system, whereas others have used the terminology free-surface shock waves to describe them, indicating an independent nonlinear nondispersive wave system. Our own present viewpoint is somewhere between the two, i.e., for sufficiently steep waves, a free-surface separation and wake region is superimposed on top of and possibly modifies the underlying dispersive wave system. The separation region is nondispersive, but diffuses and mixes with the underlying flow in the same manner as a turbulent wake. In the case of body-generated waves, strong interactions can occur with the body boundary layer, especially in the stern region, the separation regions can be quite large, and substantial modifications of the dispersive wave system are possible. For the present, we retain the terminology wave-induced separation to refer to the phenomenon exhibited in the present experiment; however, the three-dimensional separation referred to includes both the boundary layer and the free surface itself. Certainly much more work needs to be done in order to understand and develop a theory for these complicated free-surface flow structures.

## VII. CONCLUDING REMARKS

Detailed experimental information has been presented which documents the effects of waves on the boundary layer of a surface-piercing body. The effects are shown to be significant. In particular, the variations of the streamwise  $P_x$  and depthwise  $P_z$  external-flow piezometric-pressure gradients cause acceleration and deceleration phases of the streamwise velocity component and alternating direction of the cross flow which result in large oscillations of the displacement thickness and wall-shear stress as compared to the no-wave condition. For  $0 < x < .5$ ,  $P_x$  is favorable which accelerates the streamwise velocity component and results in a reduction in displacement thickness and an increase in wall-shear stress near the free surface. These effects are compounded by a favorable  $P_z$  for  $0 < x < .25$  which drives the cross flow away from the free surface and tempered by an adverse  $P_z$  for  $.25 < x < .5$  which drives the cross flow towards the free surface. For  $.5 < x < 1$ ,  $P_x$  is adverse, which decelerates the streamwise velocity component and results in an increase in displacement thickness and a reduction in wall-shear stress near the free surface. These effects are compounded by an adverse  $P_z$  for  $.5 < x < .75$  and tempered by a favorable  $P_z$  for  $.75 < x < 1$ . The magnitude of these trends increases with increasing wave steepness. Also, waves of sufficient steepness induce flow separation near the free surface in regions where  $P_x$  is adverse and the cross flow is towards the free surface. Although we were able to observe certain features of wave-induced separation and identify and discuss some relevant phenomena, it is apparent that much more work needs to be done in order to understand and develop a theory for such complex free-surface flow structures.

The measurements have been compared to the calculations of Stern (1986) and close agreement demonstrated. The computational method of approach utilizes the usual first-order boundary-layer equations with a symmetry-condition approximation for the free-surface boundary conditions. Thus, it is concluded that many features of the flow can be predicted with such an approach; however, wave-induced separation is not predicted for the large-steepness condition, although present in the experiments. As was discussed in Section V.B, in order to predict the flow very near the free surface, including wave-induced separation and the flow within the separation region, more advanced computational fluid dynamics techniques than those used presently are required



in which higher-order viscous-flow equations are solved with more exact treatment of the free-surface boundary conditions. In such a computational study, a critical issue that needs to be resolved is the determination of appropriate free-surface boundary conditions for turbulent flow, especially for conditions under which wave-induced separation occurs.

It should be recognized that we have been able to explain most of the experimental and theoretical results solely with reference to the external-flow piezometric-pressure gradients and without taking into account the free-surface boundary conditions. In the case of the calculations, this is consistent with the symmetry-condition approximation used for the free-surface boundary conditions. In the case of the experiments, this may be due to the fact that the first depthwise measurement location  $z = 5\text{cm}$  is, in most cases, greater than one boundary-layer thickness ( $\delta \sim 3\text{cm}$ ) from the free surface, and our previous work (Stern, 1986) indicates that the influence of the free-surface boundary conditions penetrates only to a depth of  $\sim \delta$ . The analogy between the present flow and the flow in a streamwise corner has already been pointed out. It should also be mentioned that, for curved corner flow, it is well known that the effects of lateral curvature are likely to be an order of magnitude larger than those due to Reynolds stress gradients (Johnston, 1978). Thus, for the present circumstances, especially for steep waves, pressure-gradient effects may predominate. However, detailed flow structures close to the free surface, such as wave-induced separation, no doubt, depend very much on the free-surface boundary conditions as well.

With regard to the direction of future work, pitot-probe wake measurements as well as boundary-layer and wake turbulence measurements using hot-film probes are planned. Also, of interest are experiments using practical hull forms in order to study the influence of body-geometry pressure-gradient and curvature effects.

## REFERENCES

- Baba, E., (1969), "A New Component of Viscous Resistance of Ships," J. Soc. Naval Arch. Japan, Vol. 125, pp. 9-34.
- Battjes, J.A. and Sakai, T., (1981), "Velocity field in a steady breaker," J. Fluid Mech., Vol. 111, pp. 421-437.
- Chow, S.K., (1967), "Free-Surface Effects on Boundary-Layer Separation on Vertical Struts," Ph.D. Thesis, The University of Iowa, Iowa City, IA.
- Doi, Y., (1980), "Observation of Stern Wave Generation," Proc. Cont. Workshop on Ship Wave Resistance, Izu Shuzenji, Japan, pp. 155-172.
- Doi, Y., Takeuchi, S., Hong, S., Kajitani, H. and Miyata, H., (1981), "Characteristics of Stern Waves Generated by Ships of Simple Hull Form (First Report)," J. Soc. Naval Arch. Japan, Vol. 150.
- Doi, Y., Takeuchi, S., Hong, S., Kajitani, H. and Miyata, H., (1982), "Characteristics of Stern Waves Generated by Ships of Simple Hull Form (Second Report)," J. Soc. Naval Arch. Japan, Vol. 151.
- Doi, Y. and Kajitani, H., (1986), "An Analysis of Waves and Viscous Flow Interaction Around Ship Form," HMRI, Korea.
- Duncan, J.H., (1983), "The breaking and non-breaking wave resistance of a two-dimensional hydrofoil," J. Fluid Mech., Vol. 126, pp. 507-520.
- Inui, T., (1981), "From Bulbous Bow to Free-Surface Shock Wave - Trends of 20 Years' Research on Ship Waves at the Tokyo University Tank," J. Ship Research, Vol. 25, No. 3, pp. 147-180.
- Johnston, J.P., (1978), "Internal Flow," Topics in Applied Physics, Springer-Verlag, Berlin, Vol. 12, pp. 109-169.
- Longuet-Higgins, M.S., (1978), "The instabilities of gravity waves on deep water I. Superharmonics and II. Subharmonics," Proc. R. Soc. Lond. A, Vol. 360, pp. 471-505.
- Longuet-Higgins, M.S. and Cokelet, E.D., (1978), "The deformation of steep surface waves on water II. Growth of normal-mode instabilities," Proc. R. Soc. Lond. A, Vol. 364, pp. 1-28.
- Mellor, G.L. and Gibson, D.M., (1966), "Equilibrium turbulent boundary layers," J. Fluid Mechanics, Vol. 24, pp. 225-253.
- Miyata, H. and Inui, T., (1984), "Nonlinear ship waves," Adv. Appl. Mech., Vol. 24, pp. 215-288.
- Mori, K., (1986), "Sub-Breaking Waves and Critical Condition for Their Appearance," Spring Meeting, Soc. Naval Arch. Japan.

Nash, J.F. and Scruggs, R.M., (1976), "An Implicit Method for the Calculation of Three-Dimensional Boundary Layers on Fuselage Configurations," Report No. 1676ER0199, Sybucon Inc., Atlanta, Georgia.

Patel, V.C. and Choi, D.H., (1979), "Calculation of Three-Dimensional Laminar and Turbulent Boundary Layers on Bodies of Revolution at Incidence," Proc. 2nd Symp. on Turbulent Shear Flow, London, pp. 170-217.

Patel, V.C., Sarda, O.P. and Shahshahan, A., (1983), "Calculation of Ship Boundary Layers," Proc. 4th Symp. on Turbulent Shear Flow, Karlsruhe, Germany, p. 3.1.

Patel, V.C. and Baek, J.H., (1985), "Calculation of Boundary Layers and Separation on a Spheroid at Incidence," AIAA J., Vol. 23, pp. 55-63.

Peregrine, D.H. and Svendsen, I.A., (1978), Proc. 16th Conf. Coastal Engng., Hamburg, Vol. 1, pp. 540-550.

Salvesen, N., (1966), "Second-Order Wave Theory for Submerged Two-Dimensional Bodies," Proc. 6th ONR Symp. Naval Hydrodynamics, Washington, D.C., pp. 25:1-25:34.

Salvesen, N., (1969), "On Higher-Order Wave Theory for Submerged Two-Dimensional Bodies," J. Fluid Mech., Vol. 38, Part 2, pp. 415-432.

Salvesen, N. and von Kerczek, C.H., (1975), "Numerical Solutions of Two-Dimensional Nonlinear Body-Wave Problems," Proc. 1st Int. Conf. Num. Ship Hydrodynamics, Washington, D.C., pp. 279-293.

Stern, F., (1985), "The Influence of Wavemaking by Surface-Piercing Bodies on Their Boundary-Layer Development," Proc. 4th Int. Conf. on Num. Ship Hydro., Washington, D.C., pp. 383-406.

Stern, F., (1986), "Effects of Waves on the Boundary Layer of a Surface-Piercing Body," J. Ship Res., Vol. 30, No. 4, pp. 256-274.

Stokes, G.G., (1880), Supplement to a paper on the theory of oscillatory waves, Mathematical and Physical Papers, Cambridge U. Press, Vol. 1, pp. 314-326.

White, F.M., (1974), "Viscous fluid flow," McGraw-Hill, New York.

Yuen, H.C. and Lake, B.M., (1980), "Instabilities of Waves on Deep Water," Ann. Rev. Fluid Mech., Vol. 12, pp. 303-334.

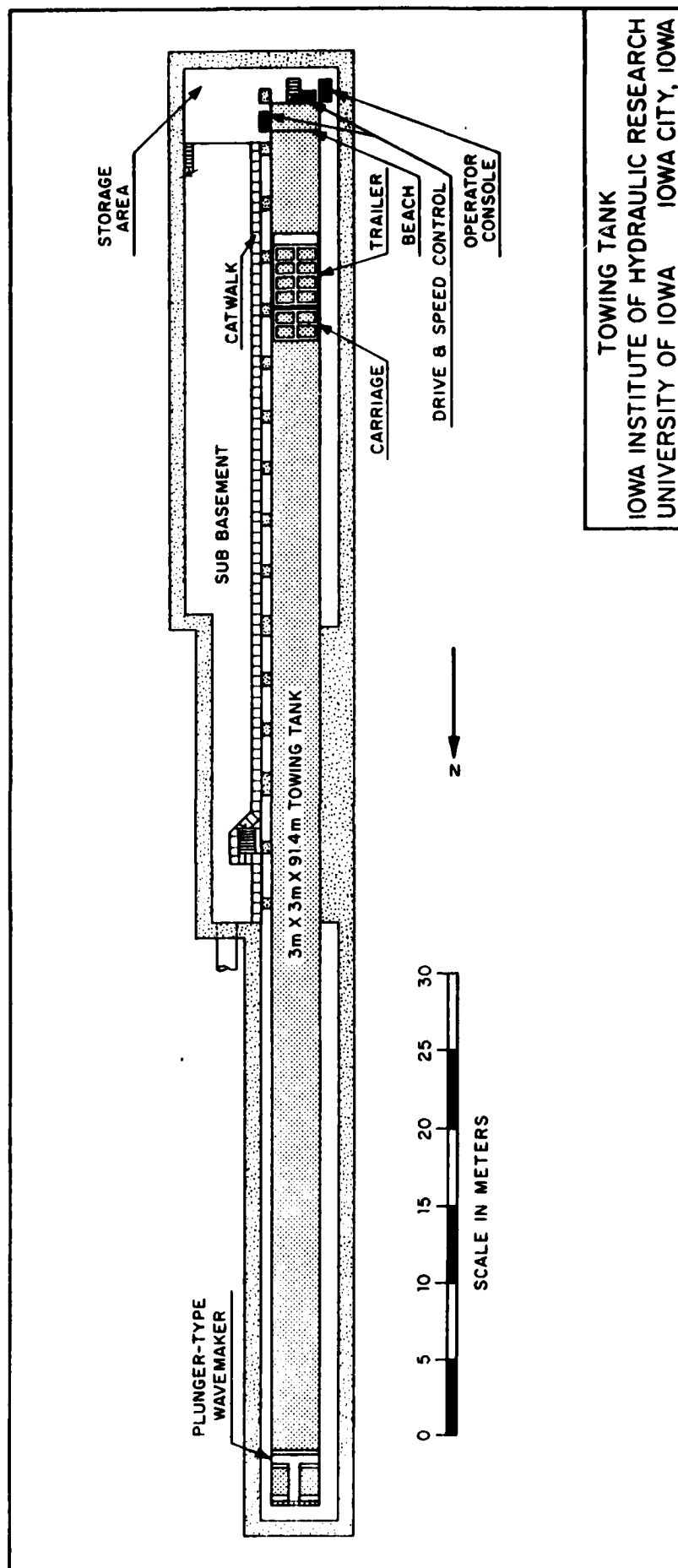


Figure 1. IIHR towing tank.



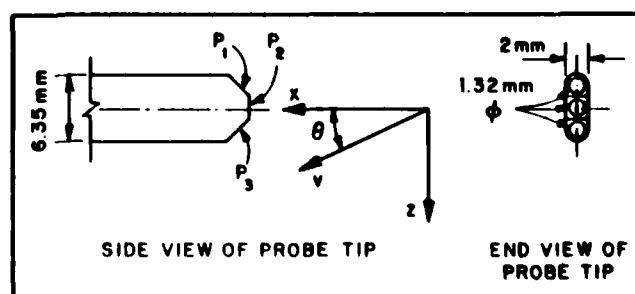
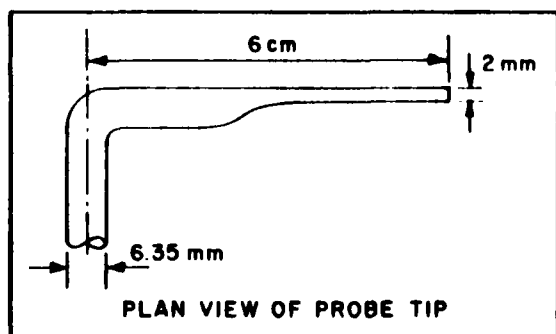
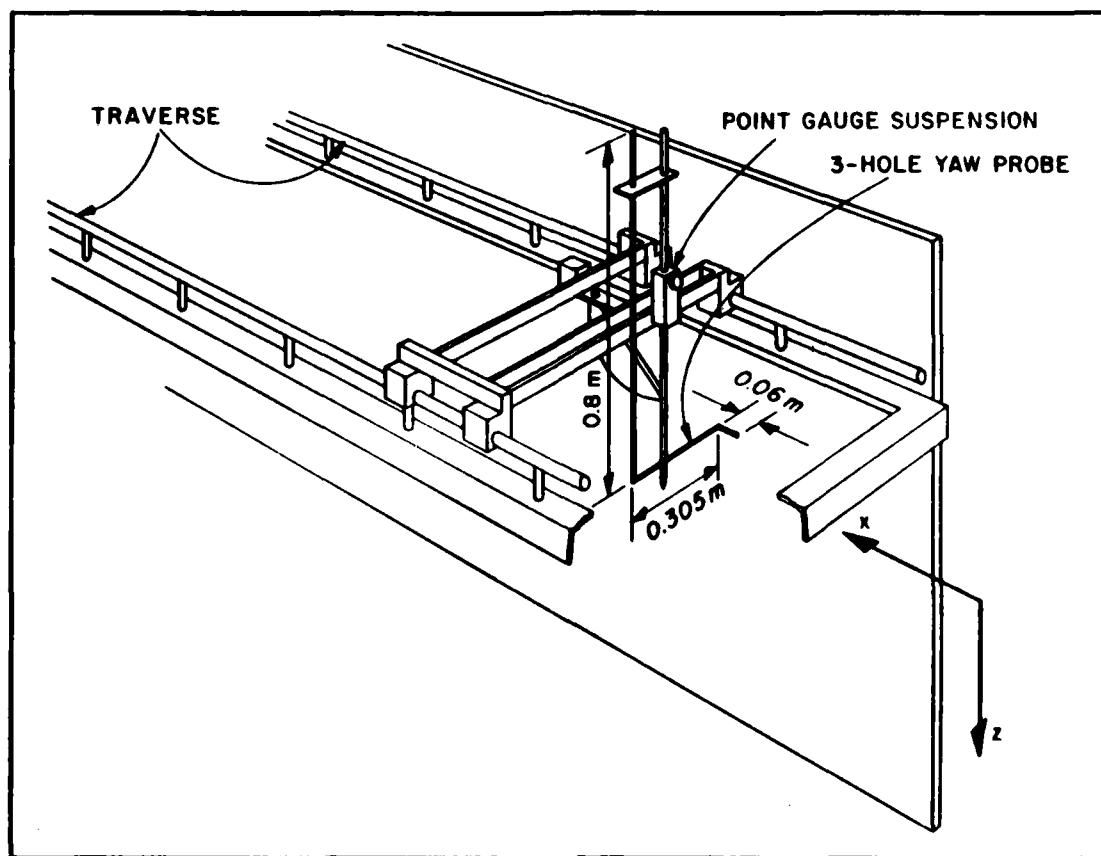


Figure 4. Three-hole yaw probe.

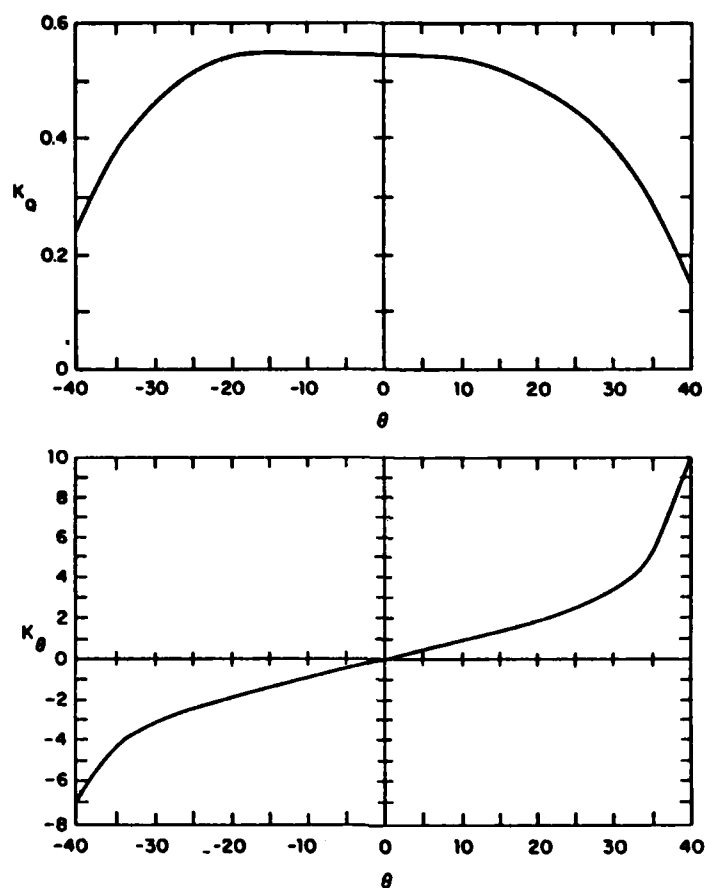


Figure 5. Calibration coefficients.

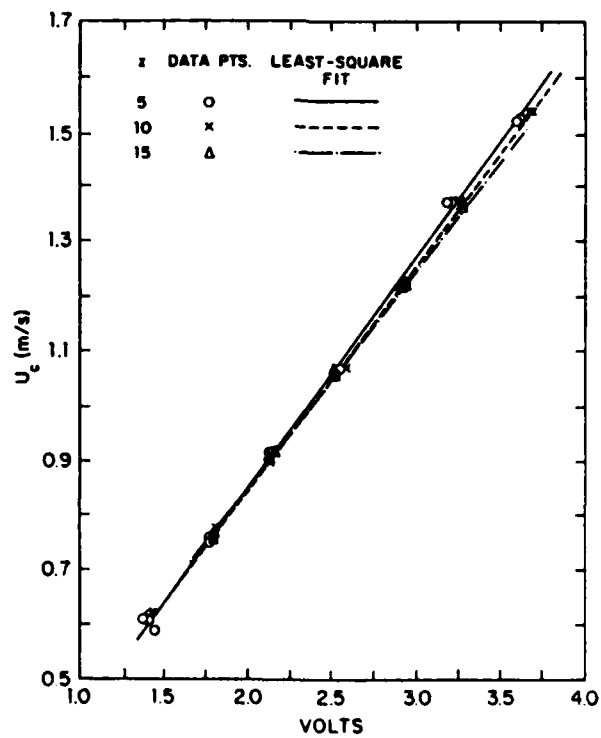


Figure 6. Dynamic calibration lines.

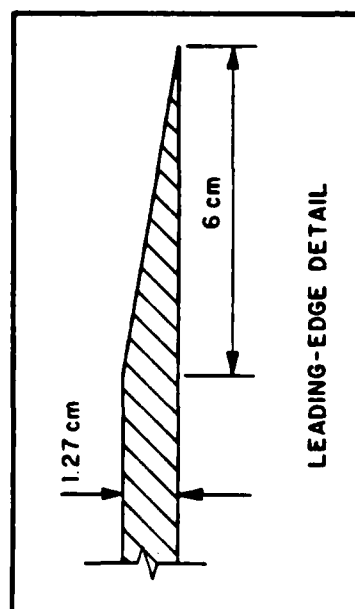
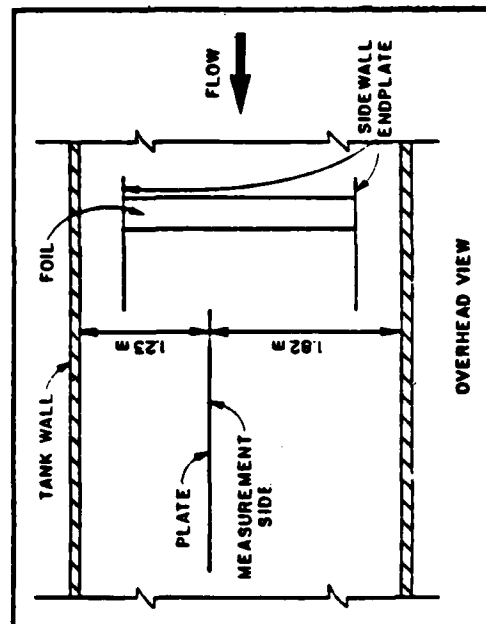
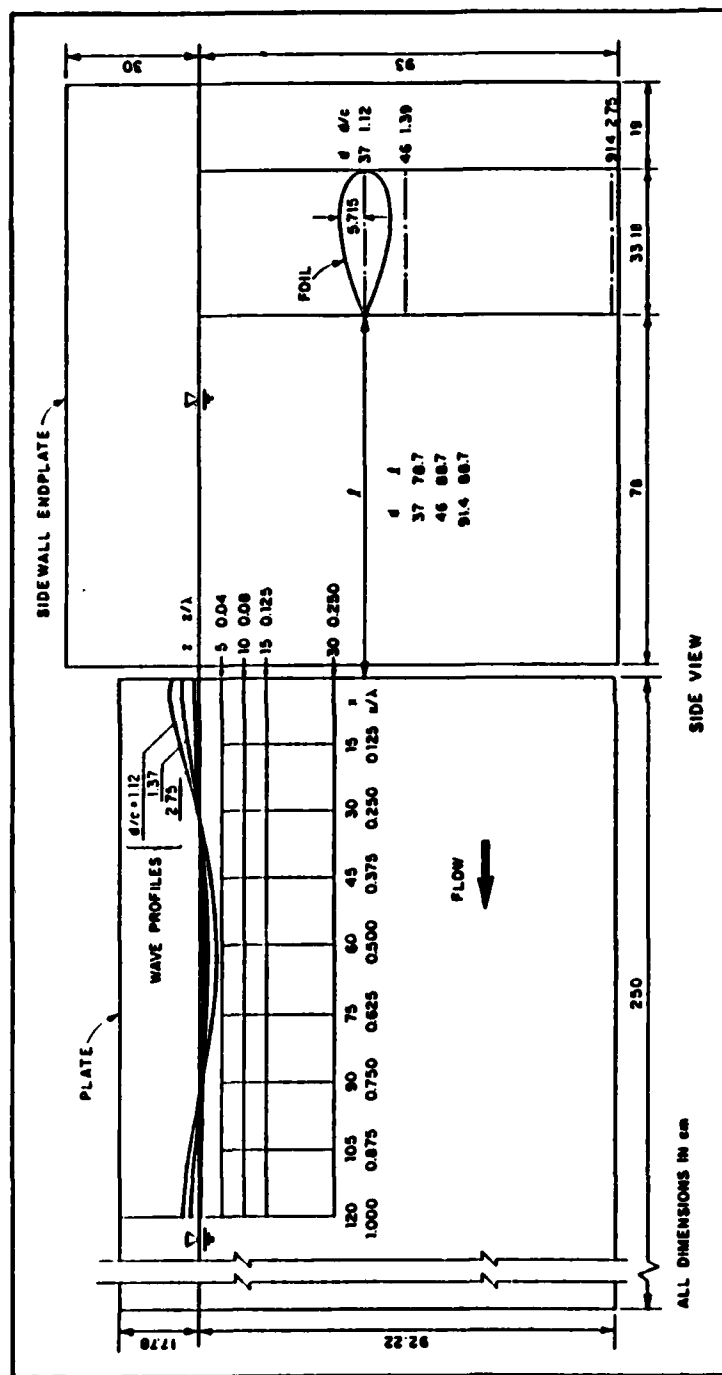


Figure 7. Measurement locations, plate positions, and foil submergence depths.



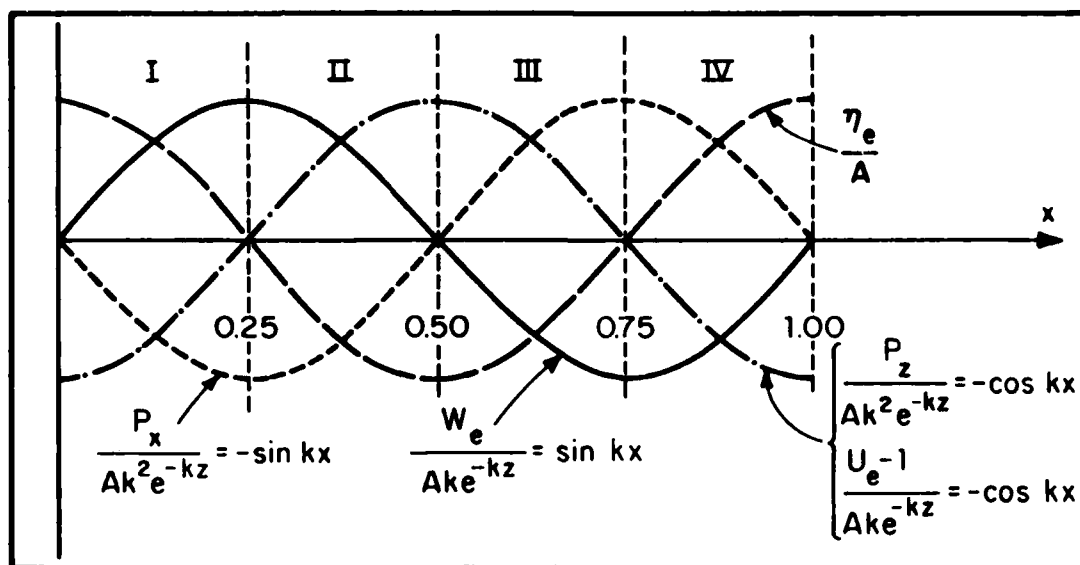


Figure 8. Potential-flow regions.

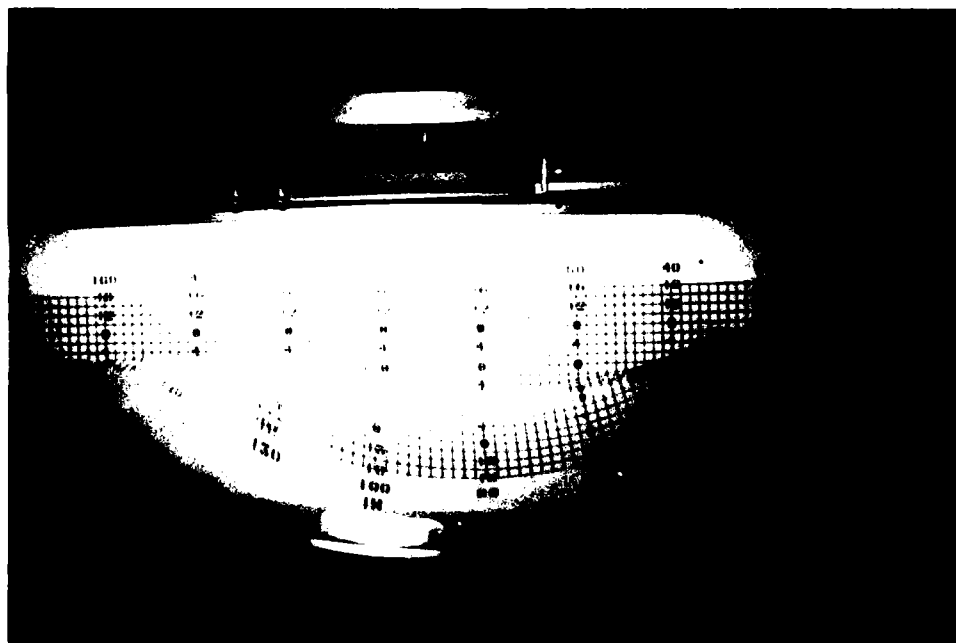


Figure 9. Wave profile:  $U_c = 1.37\text{m/s}$ ,  $d/c = 1.12$ .

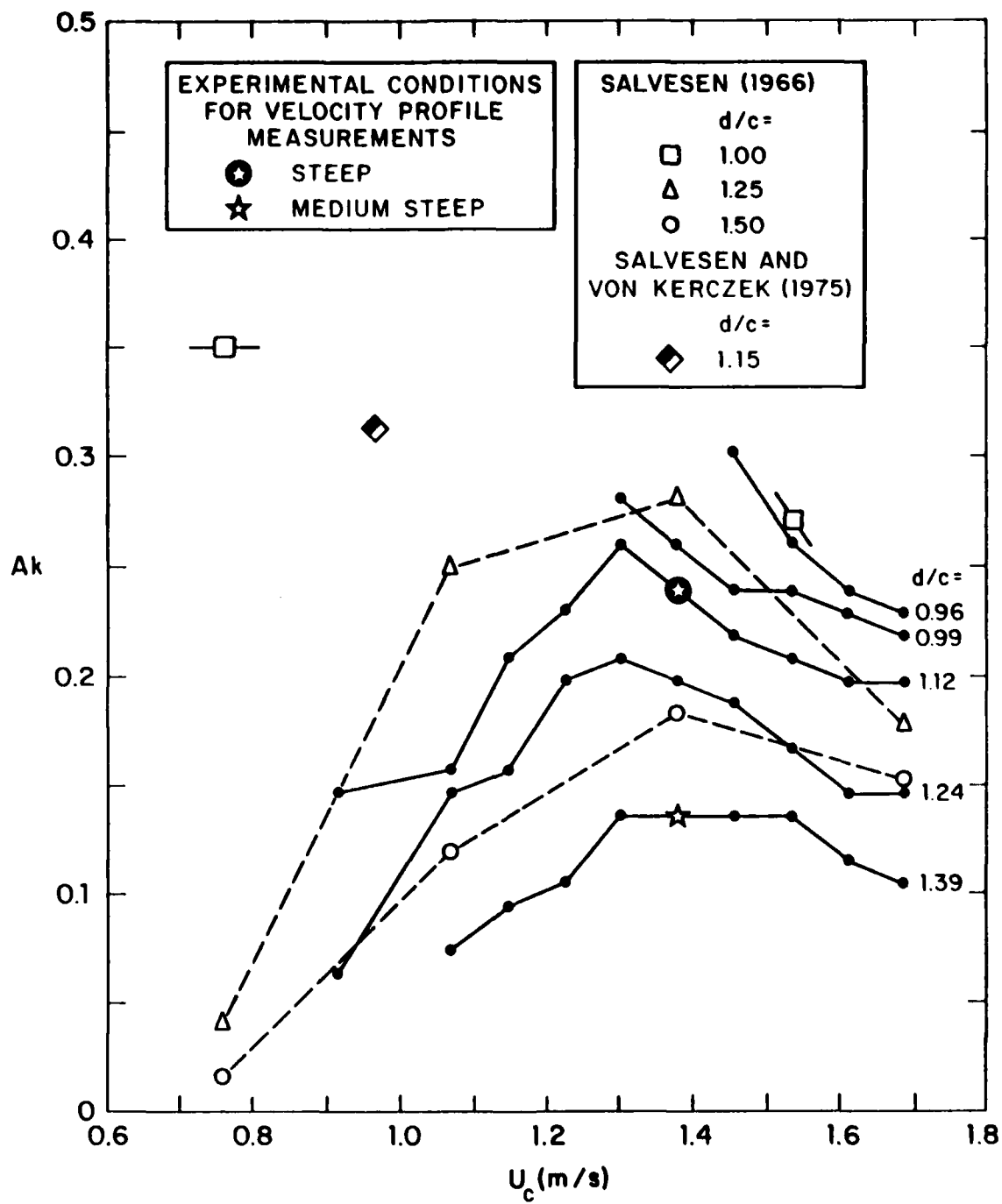
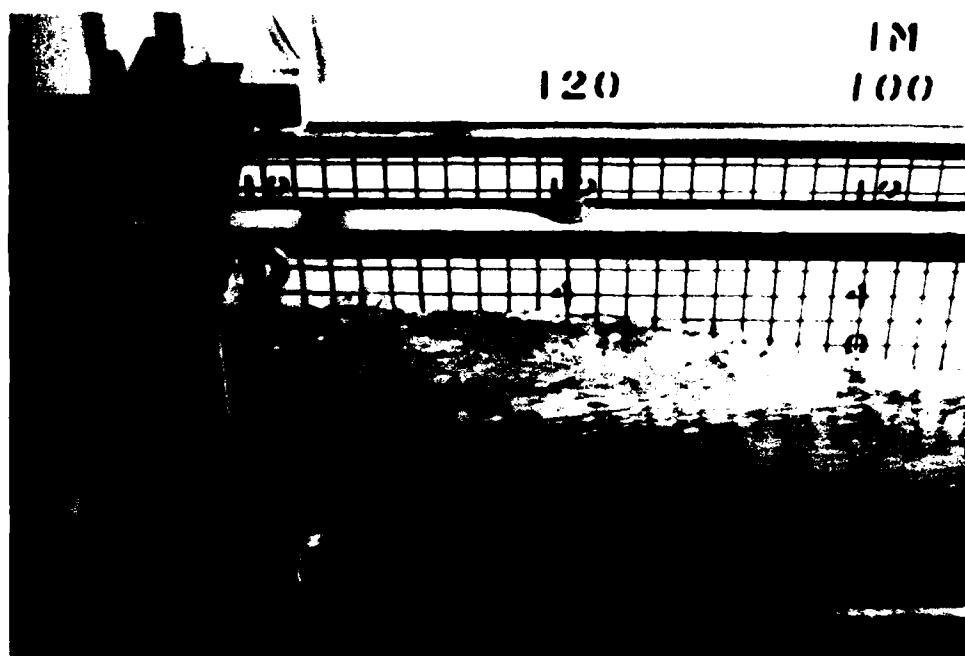
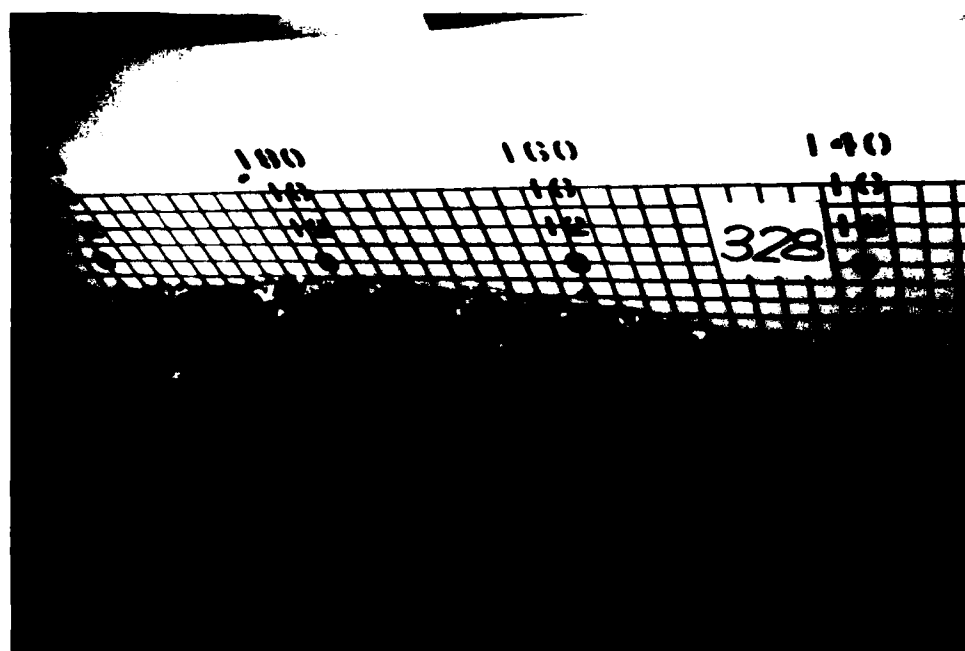


Figure 10. Wave steepness.



(a)



(b)

Figure 11. Separation pattern: (a)  $U_c = 1.37\text{m/s}$ ,  $d/c = 1.12$ ;  
 (b)  $U_c = 1.6\text{m/s}$ ,  $d/c = .96$ .

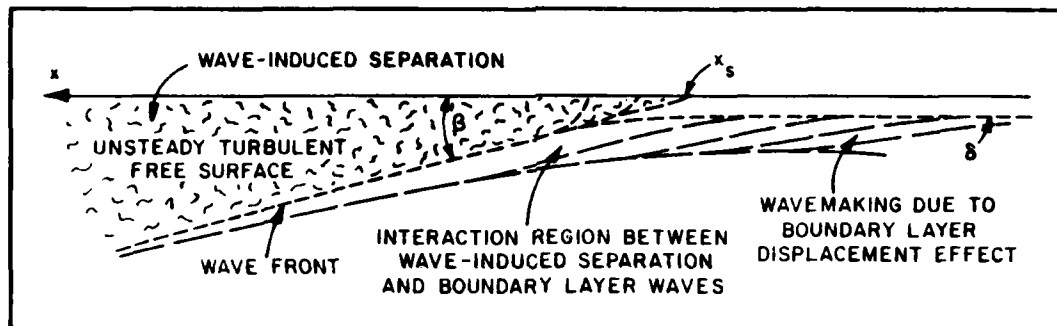


Figure 12. Wave-induced separation.

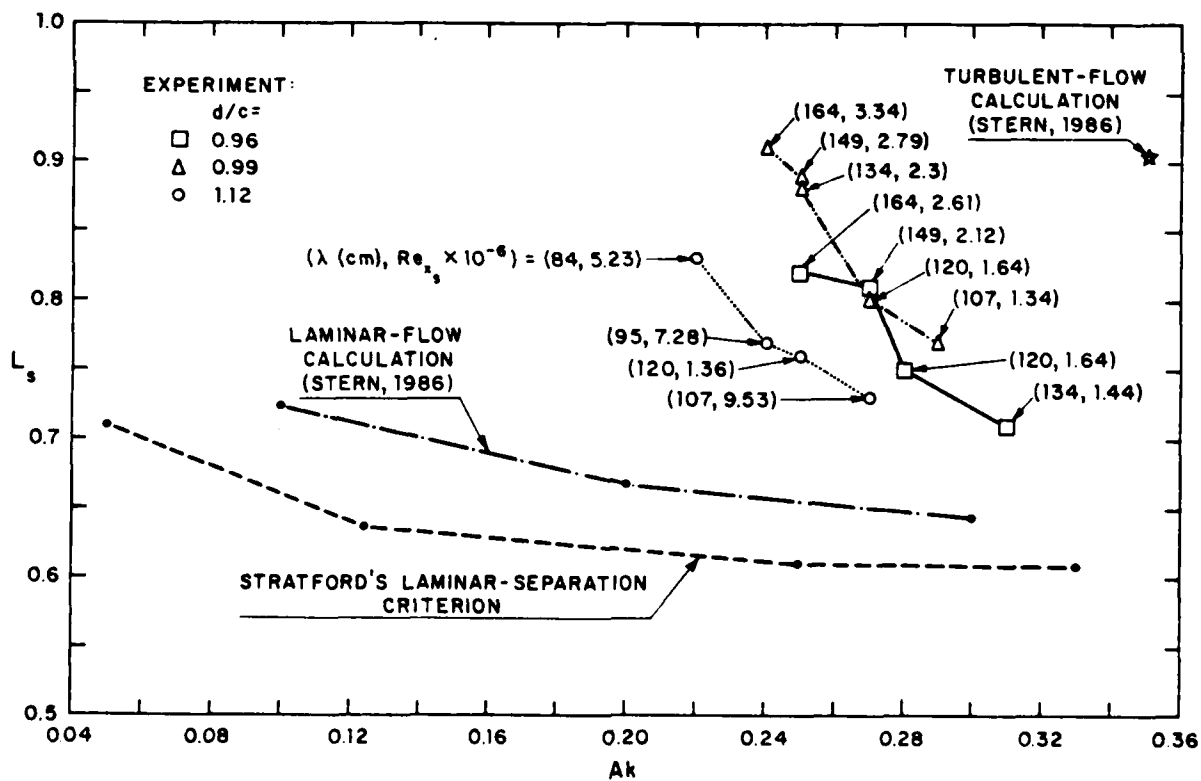


Figure 13. Separation starting point.

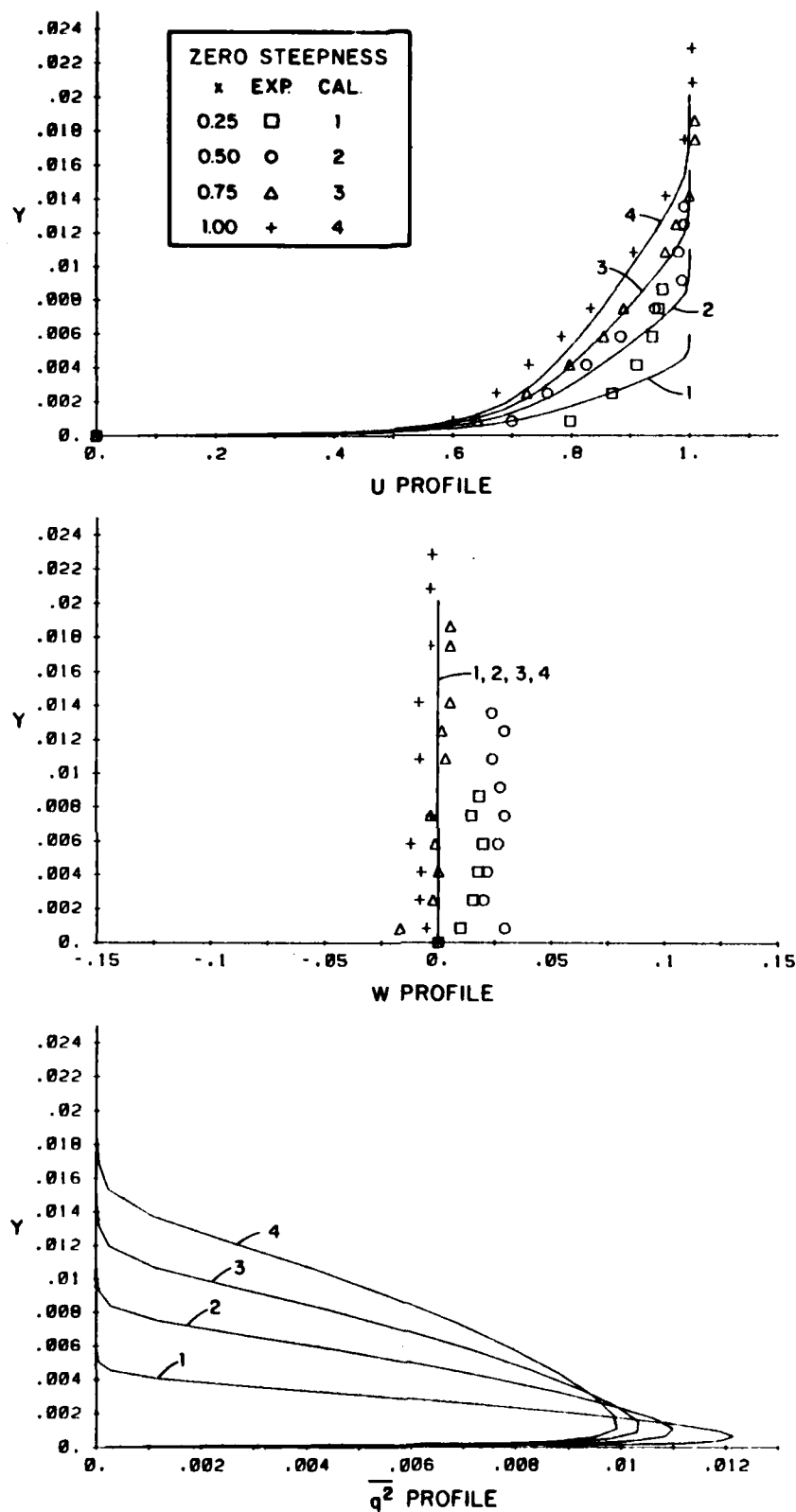


Figure 14. Velocity and turbulence-intensity profiles: zero steepness.

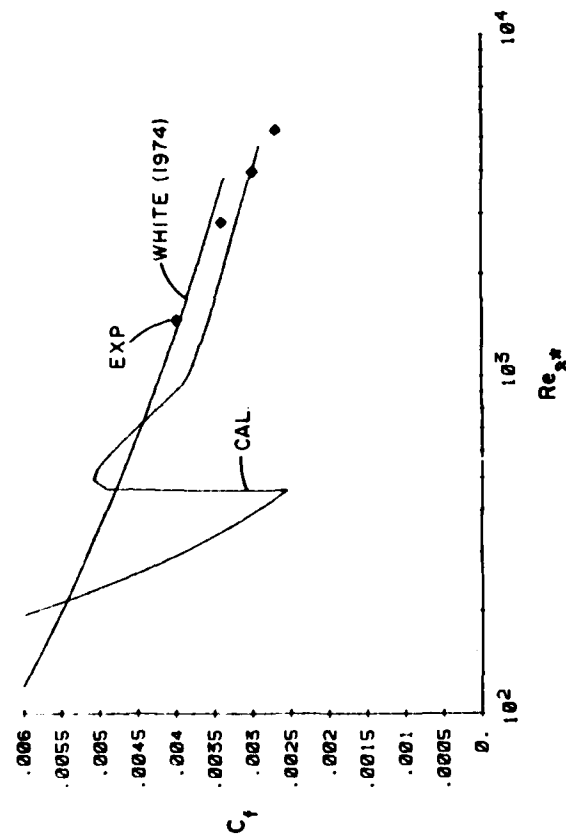


Figure 15. Wall-shear-stress magnitude: zero steepness.

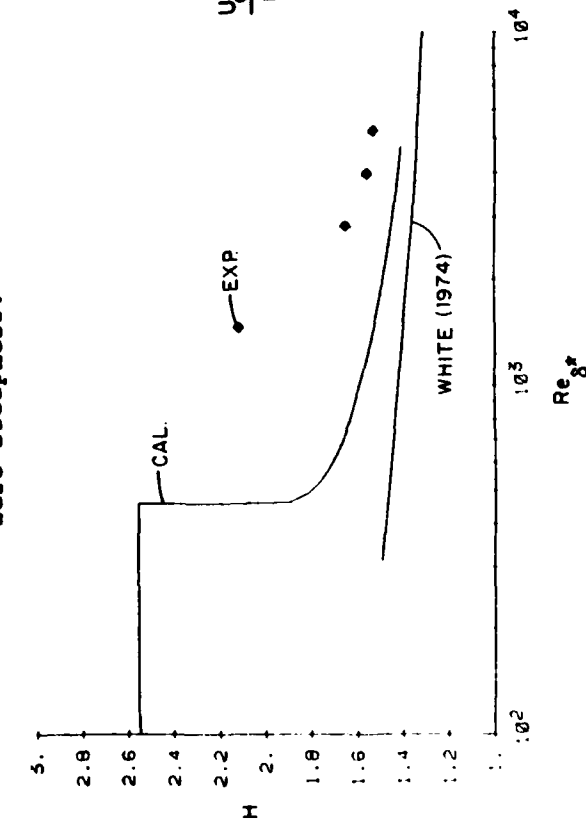


Figure 16. Shape parameter: zero steepness.

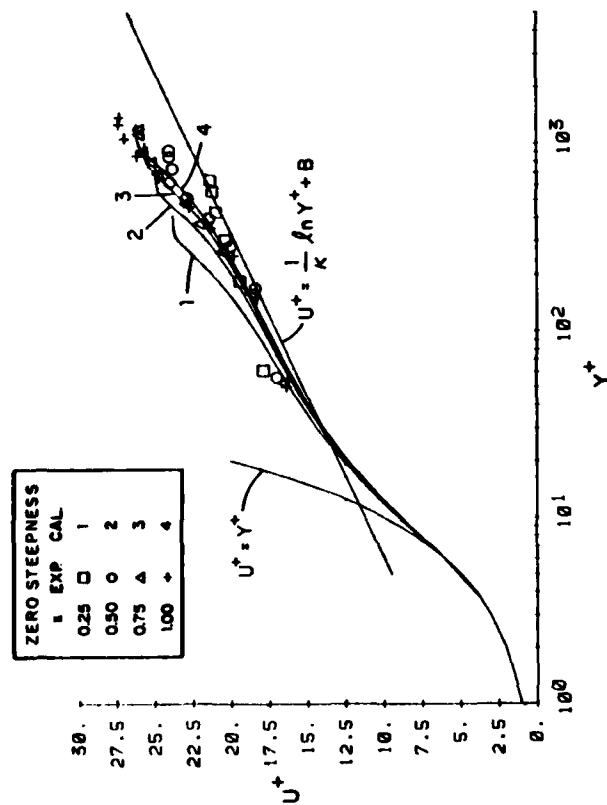


Figure 17. Velocity profiles using inner-law variables: zero steepness.

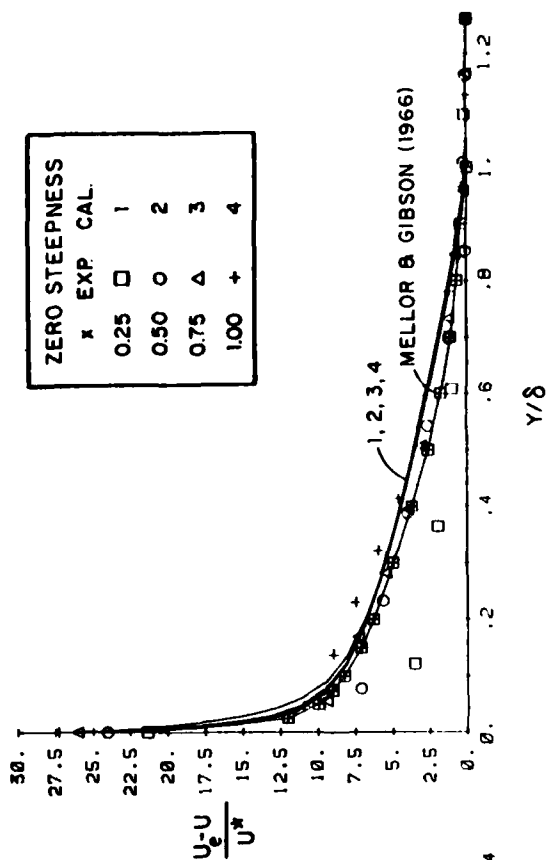


Figure 18. Velocity profiles using outer-law variables: zero steepness.

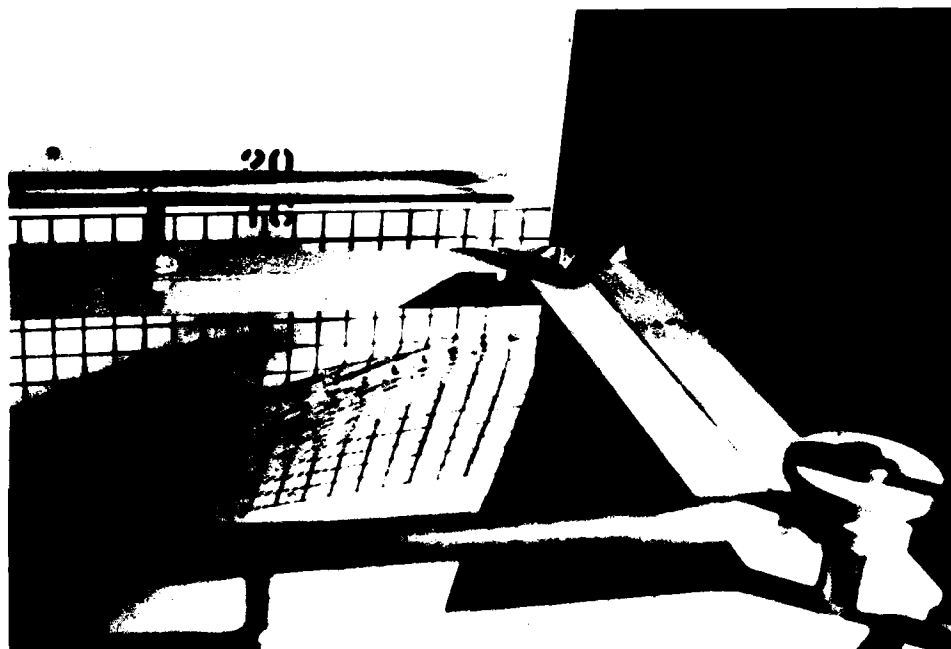


Figure 19. Leading-edge flow:  $U_c = 1.37\text{m/s}$ ,  $d/c = 1.12$ .

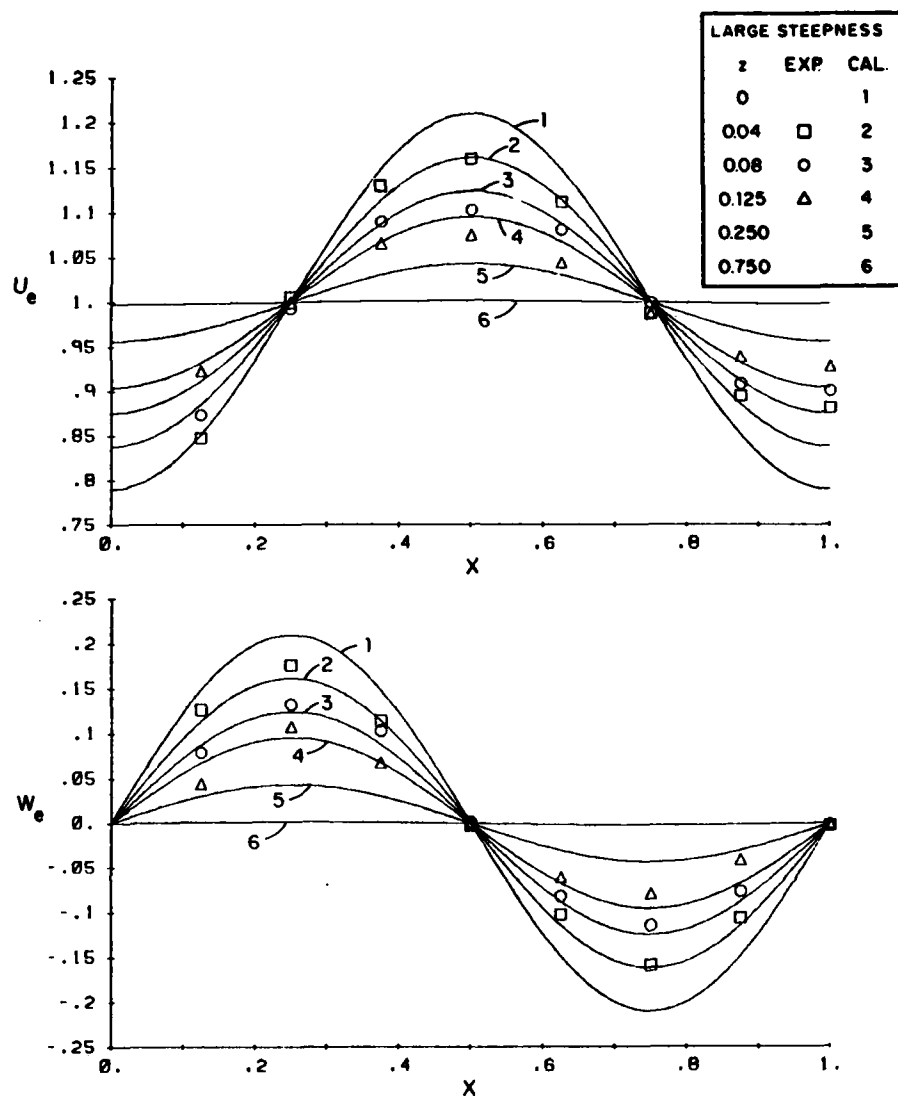


Figure 20. Edge velocity: large steepness.

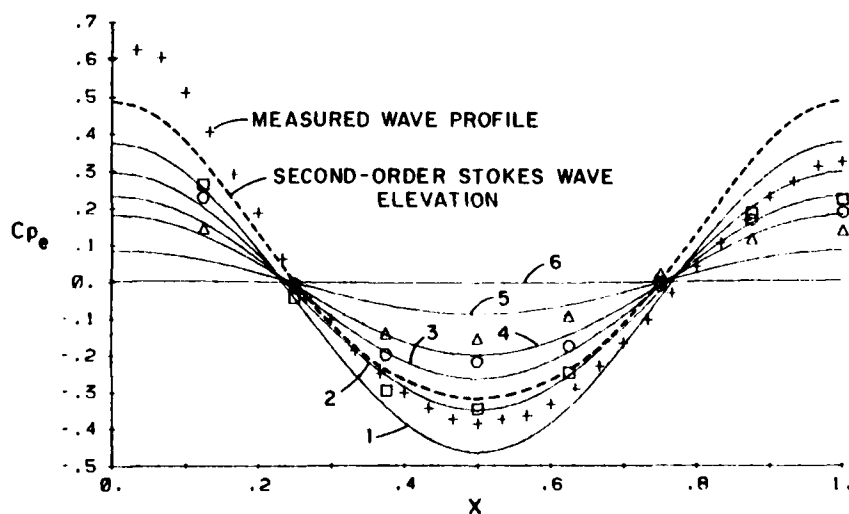


Figure 21. Edge pressure: large steepness.



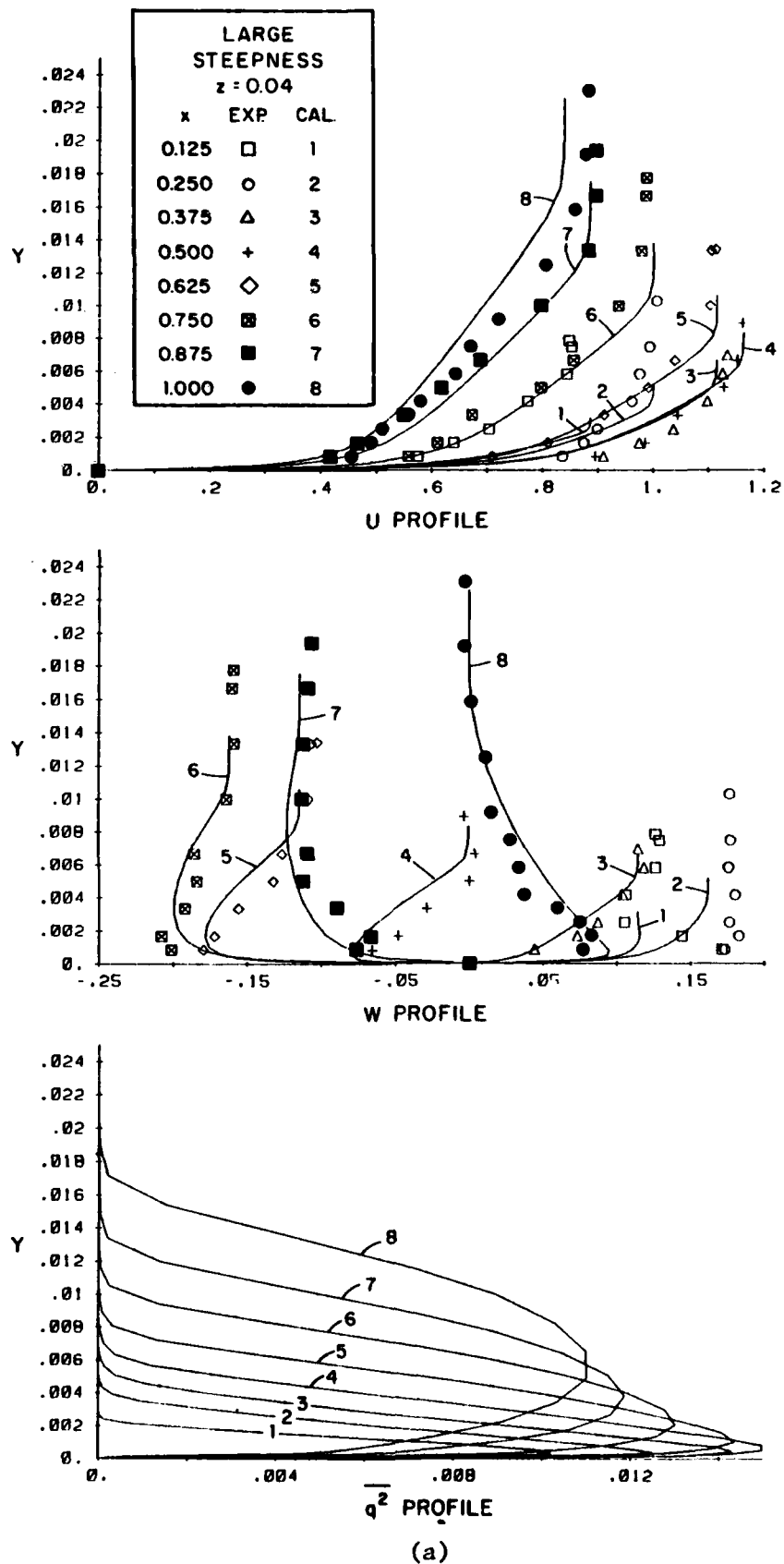
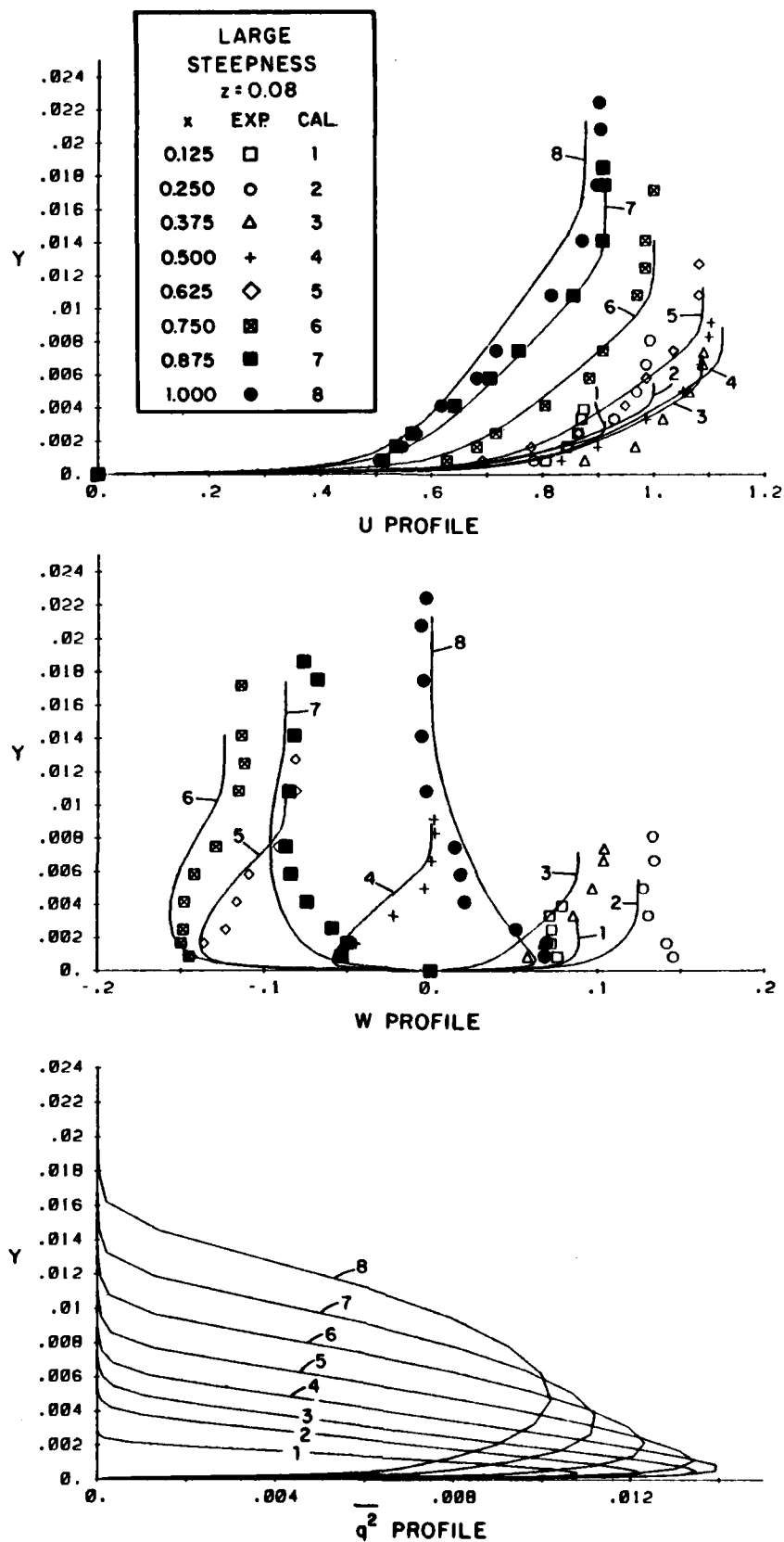


Figure 22. Velocity and turbulence-intensity profiles:  
large steepness.



(b)

Figure 22. (continued)

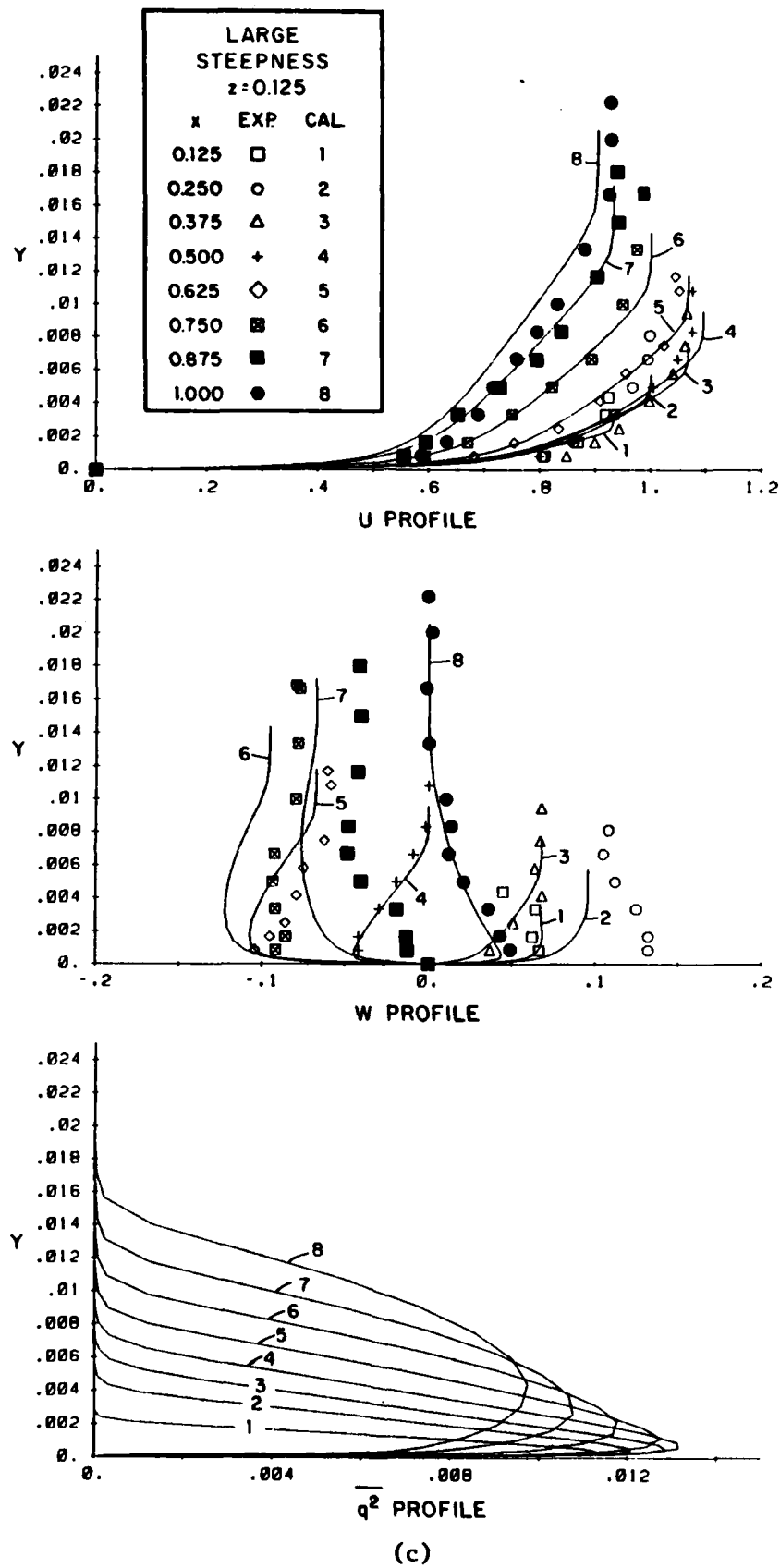


Figure 22. (continued)

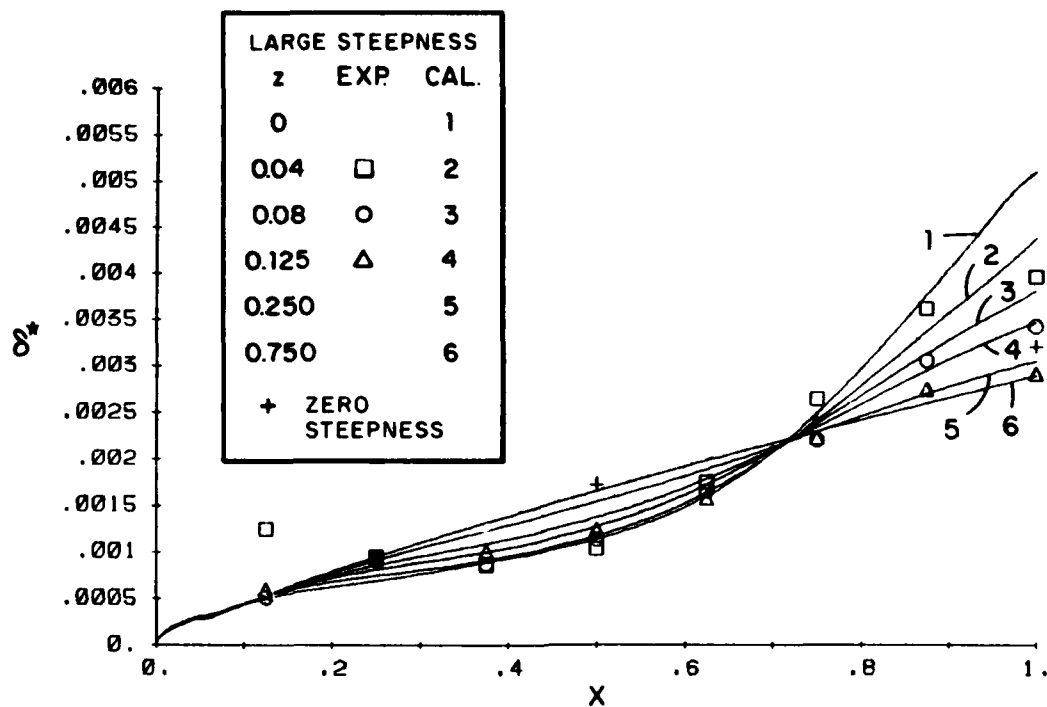


Figure 23. Streamwise displacement thickness: large steepness.

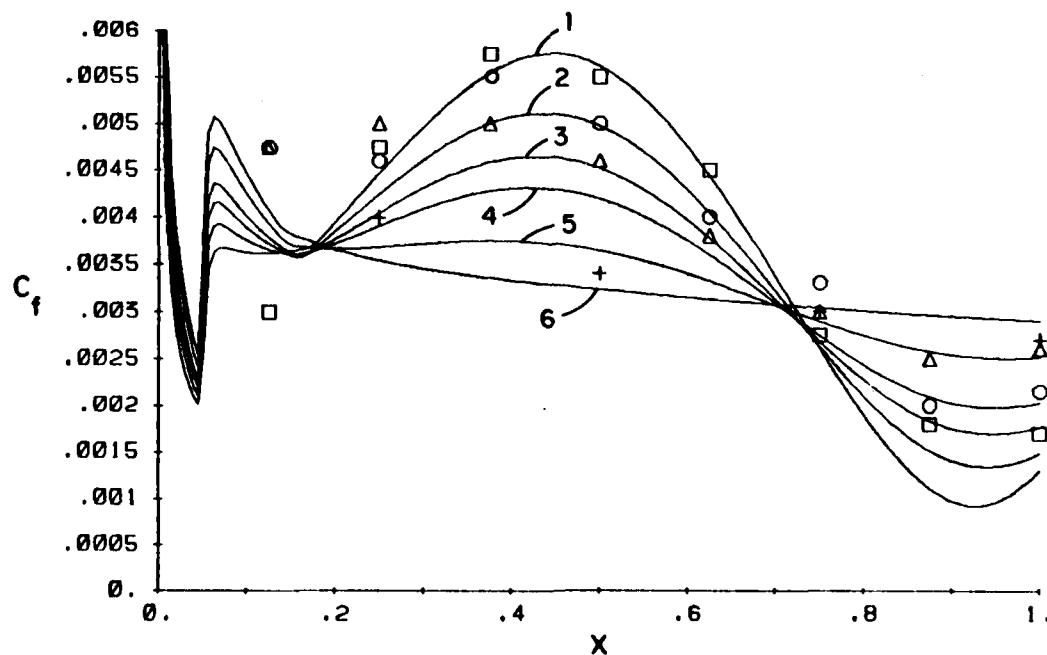


Figure 24. Wall-shear-stress magnitude: large steepness.

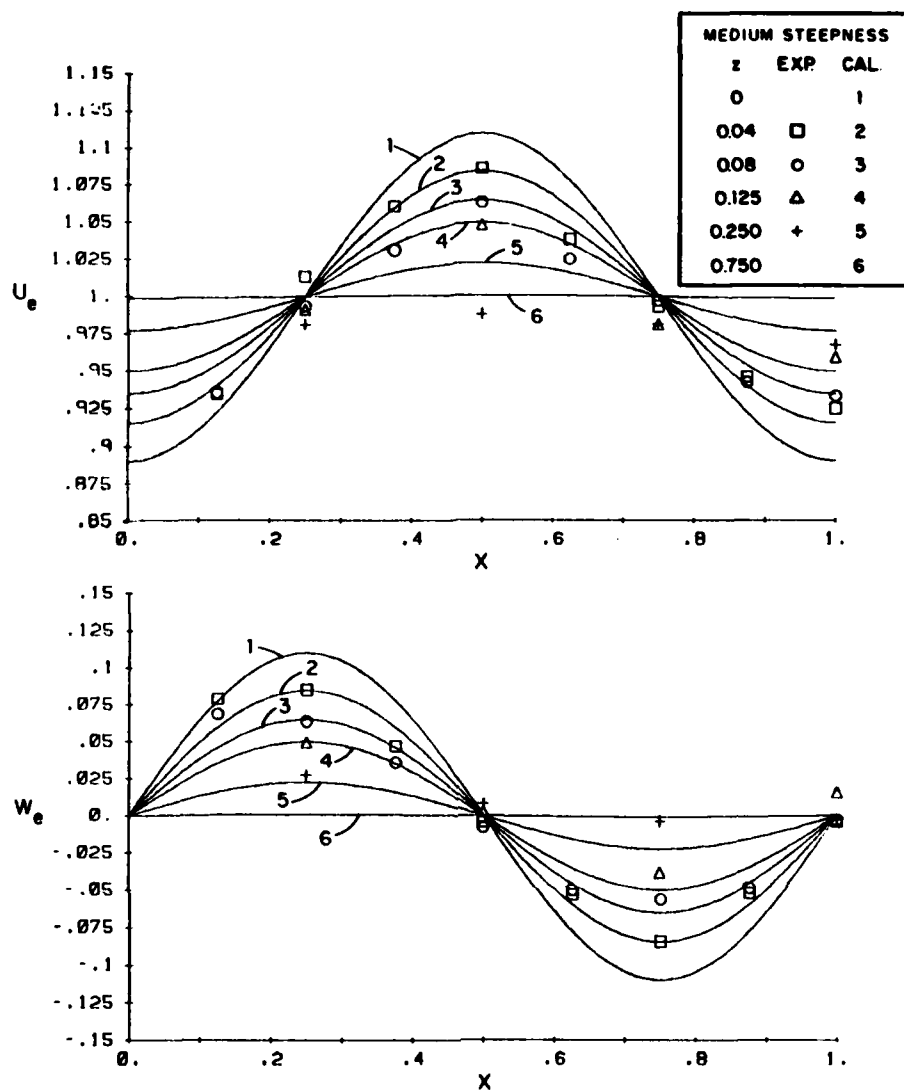


Figure 25. Edge velocity: medium steepness.

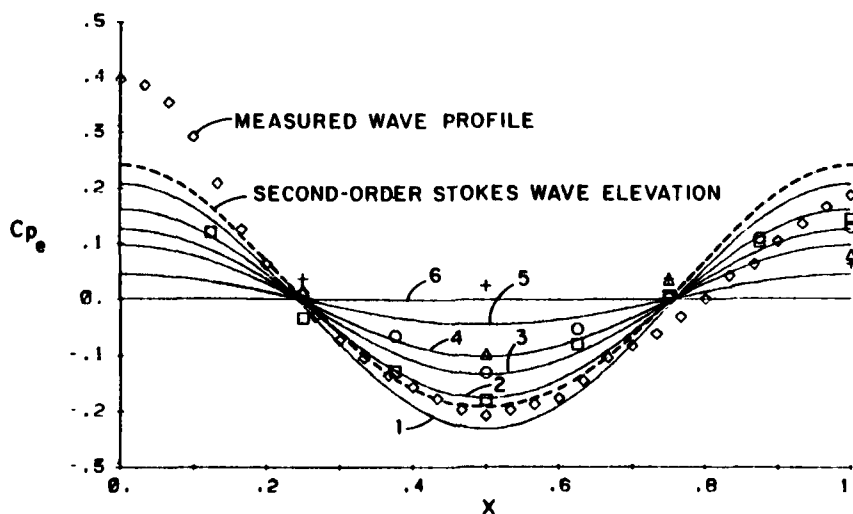


Figure 26. Edge pressure: medium steepness.

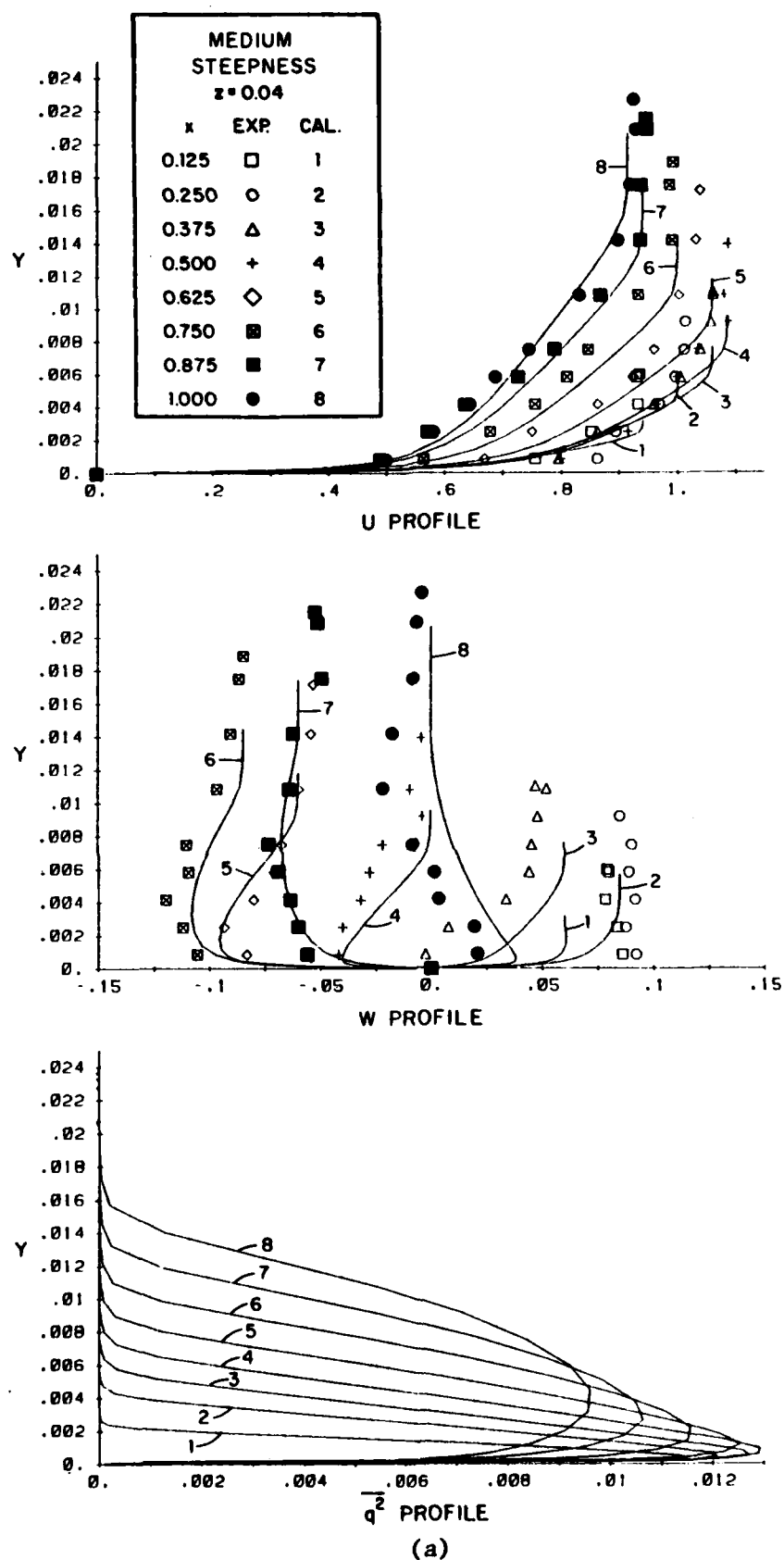


Figure 27. Velocity and turbulence-intensity profiles:  
medium steepness.

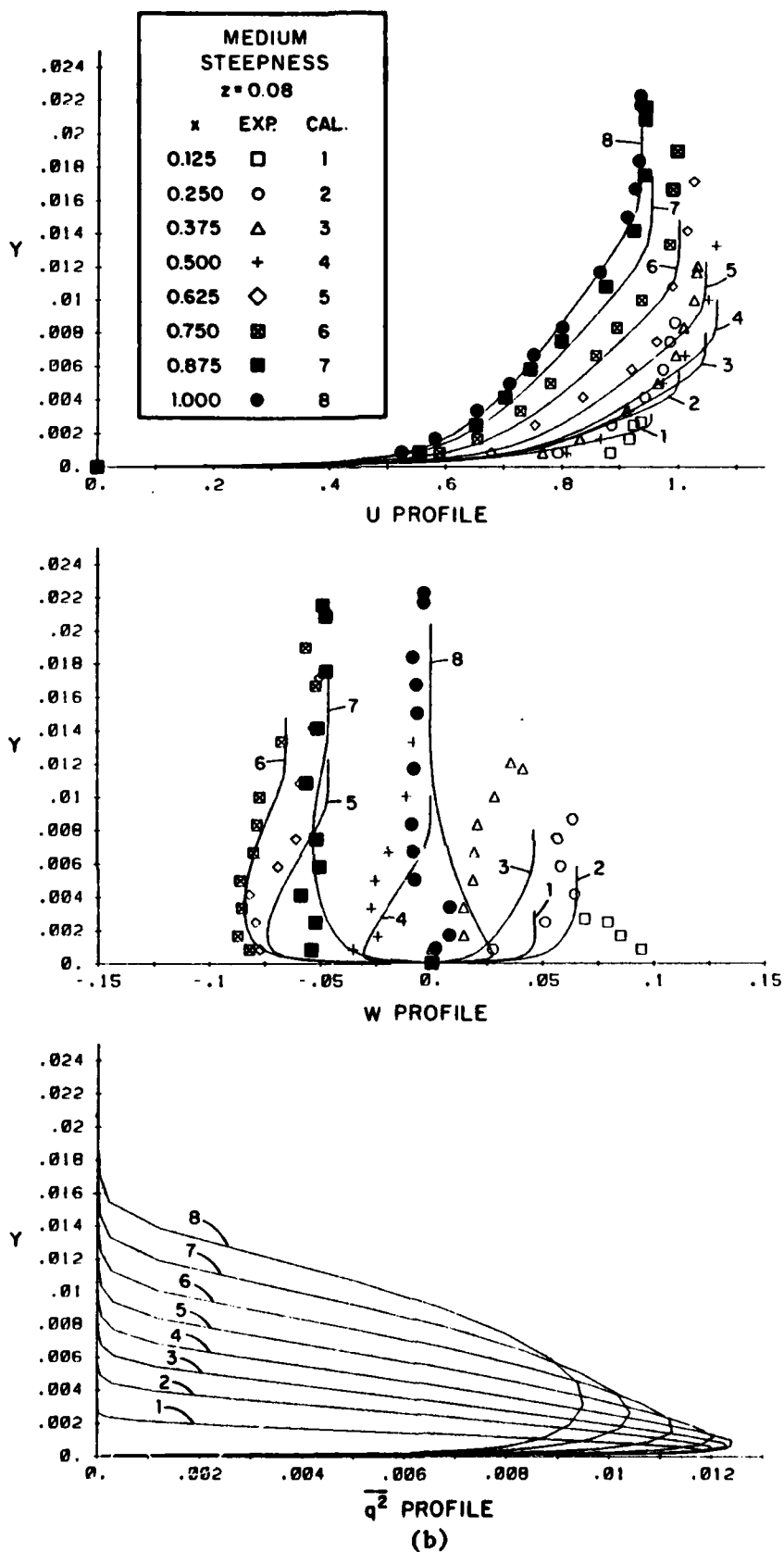


Figure 27. (continued).

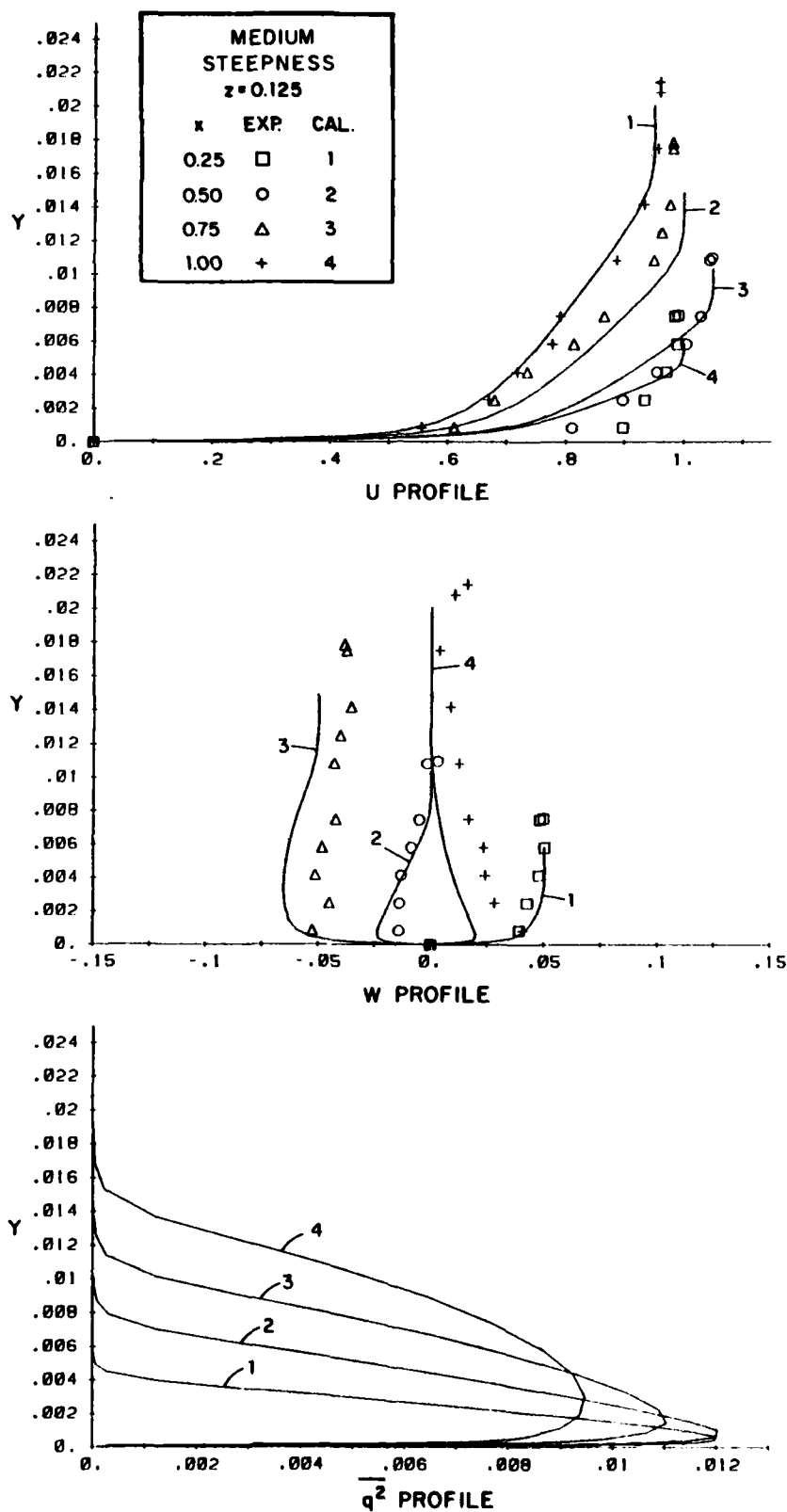


Figure 27. (continued).



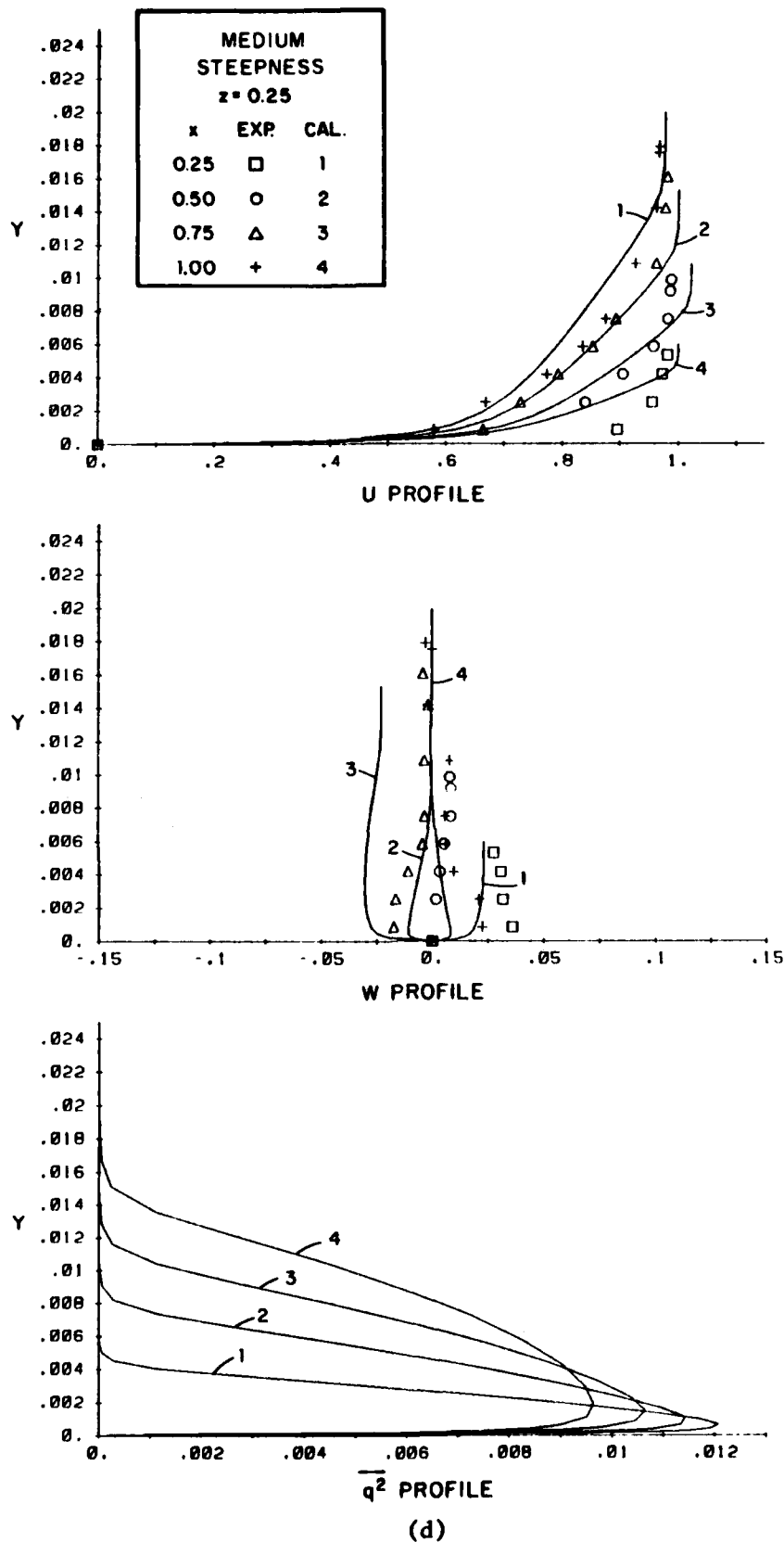


Figure 27. (continued).

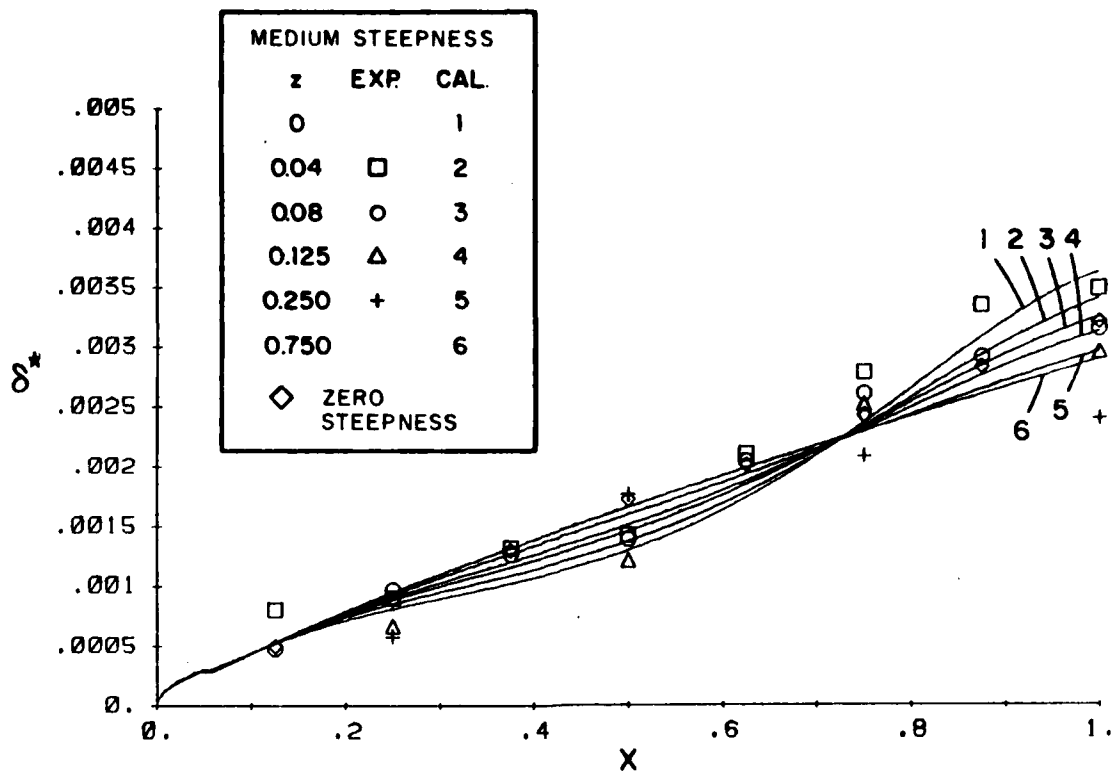


Figure 28. Streamwise displacement thickness: medium steepness.

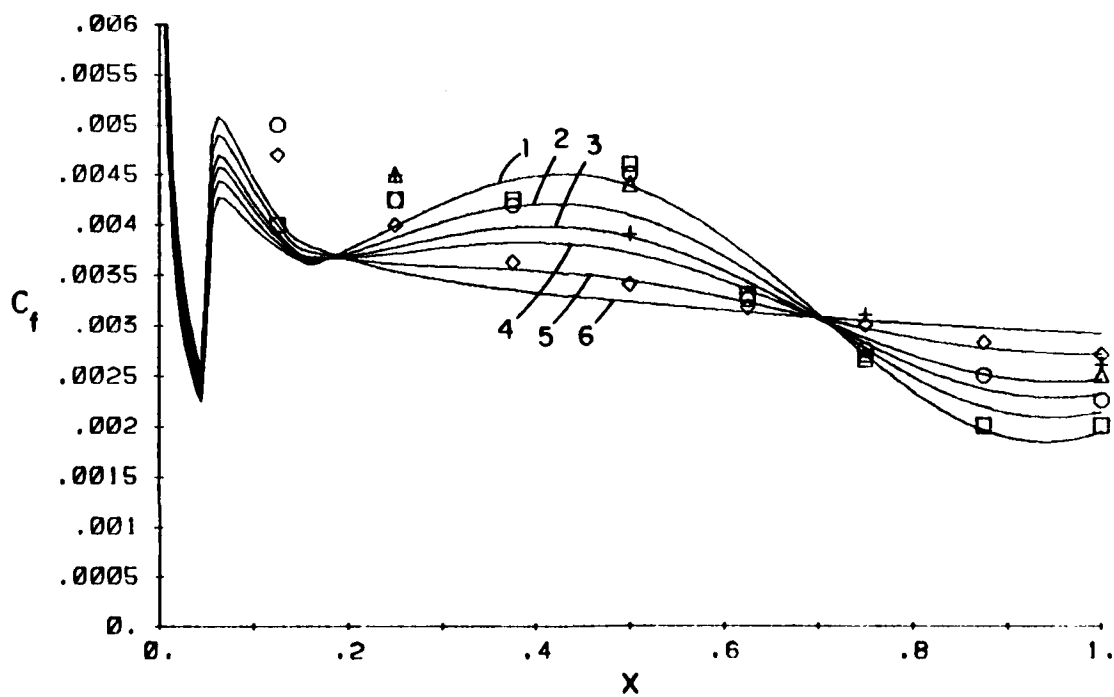


Figure 29. Wall-shear-stress magnitude: medium steepness.

DISTRIBUTION LIST FOR TECHNICAL REPORTS  
ONR FLUID DYNAMICS PROGRAM (HYDRODYNAMICS)

Defense Technical Information  
Center  
Information Facility  
Alexandria, VA 22314  
12 copies

NASA Scientific and Technical  
Information Facility  
P.O. Box 8757  
Baltimore/Washington  
International Airport  
Maryland 21240

Office of Naval Research  
Code 432F  
800 N. Quincy Street  
Arlington, VA 22217  
3 copies

Professor Bruce Johnson  
U.S. Naval Academy  
Hydromechanics Laboratory  
Annapolis, MD 21402

Library  
David Taylor Naval Ship Research  
and Development Center  
Code 522.1  
Bethesda, MD 20084

Library  
U.S. Naval Academy  
Annapolis, MD 21402

The Society of Naval Architects and  
Marine Engineers  
One World Trade Center, Suite 1369  
New York, NY 10048

Technical Library  
Naval Coastal System Center  
Panama City, FL 32401

Technical Library  
Naval Ship Engineering Center  
Philadelphia Division  
Philadelphia, PA 19112

Naval Research Laboratory  
Code 2627  
Washington, DC 20375

Library  
Naval Sea Systems Command  
Code 09GS  
Washington, DC 20362

Dr. O.M. Griffin  
Code 5841  
Naval Research Laboratory  
Washington, DC 20375

Dr. T.F. Zien  
Code R44  
Naval Surface Weapons Center  
White Oak Lab.  
Silver Spring, MD 20910

Dr. W.K. Blake  
Code 1905.1  
DTNSRDC  
Bethesda, MD 20854

Dr. T.T. Huang  
Code 1542  
DTNSRDC  
Bethesda, MD 20084

Dr. E.P. Rood  
Code 1543  
DTNSRDC  
Bethesda, MD 20084

Prof. T. Sarpkaya  
Dept. of Mechanical Engineering  
Code 69-SL  
Naval Postgraduate School  
Monterey, CA 93940

Dr. W.C. Lin  
Code 152  
DTNSRDC  
Bethesda, MD 20084

Mr. J.H. McCarthy  
Code 154  
DTNSRDC  
Bethesda, MD 20084

Mr. D.S. Cieslowski  
Code 156  
DTNSRDC  
Bethesda, MD 20084

Mr. V.J. Monacella  
Code 1504  
DTNSRDC  
Bethesda, MD 20084

Dr. B. Yim  
Code 154.1  
DTNSRDC  
Bethesda, MD 20084

Dr. Hans Lugt  
Code 1802  
DTNSRDC  
Bethesda, MD 20084

Dr. H. Haussling  
Code 1843  
DTNSRDC  
Bethesda, MD 22084

Mr. W.C. Sandberg  
Code 55W33  
Naval Sea Systems Command  
Washington, DC 20362

Mr. E.N. Comstock  
Code 55W3  
Naval Sea Systems Command  
Washington, DC 20362

Dr. A.L. Slafkosky  
Scientific Advisor  
Commandant of the Marine Corps  
Code AX  
Washington, DC 20380

Maritime Administration  
Office of Maritime Technology  
14th & E Streets, NW  
Washington, DC 20230

Maritime Administration  
Division of Naval Architecture  
14th & E Streets, NW  
Washington, DC 20230

Lorenz G. Straub Library  
University of Minnesota  
St. Anthony Falls Hydraulic  
Laboratory  
Minneapolis, MN 55414

Technical Library  
Naval Ocean Systems Center  
San Diego, CA 92152

Librarian  
University of California  
Department of Naval  
Architecture and Offshore  
Engineering  
Berkeley, CA 94720

Technical Library  
Webb Institute of Naval  
Architecture  
Glen Cove, NY 11542

Library  
Stevens Institute of Tech.  
Davidson Laboratory  
Castle Point Station  
Hoboken, NJ 07030

R.E. Gibson Library  
The Johns Hopkins University  
Applied Physics Laboratory  
Johns Hopkins Road  
Laurel, MD 20810

Library  
Naval Postgraduate School  
Monterey, CA 93940

Librarian  
Naval Surface Weapons Center  
White Oak Laboratory  
Silver Spring, MD 20910

Technical Library  
Naval Underwater Systems  
Center  
Newport, RI 02840

Library  
Department of Ocean  
Engineering  
Massachusetts Institute of  
Technology  
Cambridge, MA 01778

Engineering Societies Library  
345 East 47th Street  
New York, NY 10017

Library  
Dept. of Naval Architecture  
and Marine Engineering  
University of Michigan  
Ann Arbor, MI 48109

Librarian Station 5-2  
Coast Guard Headquarters  
NASSIF Building  
400 Seventh Street, SW  
Washington, DC 20591

Library  
Applied Research Laboratory  
The Pennsylvania State University  
P.O. Box 30  
State College, PA 16801

Library of Congress  
Science and Technology Division  
Washington, DC 20540

Library  
Marine Physical Laboratory  
Scripps Institution of Oceanography  
University of California @ San Diego  
San Diego, CA 92152

Library  
Applied Research Laboratories  
University of Texas at Austin  
Austin, TX 78712

Library  
Woods Hole Oceanographic Institution  
Woods Hole, MA 02543

Editor  
Applied Mechanics Review  
Southwest Research Institute  
8500 Culebra Road  
San Antonio, TX 78206

Library  
Institute of Hydraulic Research  
The University of Iowa  
Iowa City, IA 52242

Library  
Southwest Research Institute  
8500 Culebra Road  
San Antonio, TX 78228

Professor Robert E. Falco  
Michigan State University  
Department of Mechanical Engineering  
East Lansing, MI 48824

Mr. Dennis Bushnell  
NASA Langley Research Center  
Langley Station  
Hampton, VA 23365

Dr. A.K.M. Fazle Hussain  
University of Houston  
Department of Mechanical Engineering  
Houston, TX 77004

Professor John L. Lumley  
Cornell University  
Sibley School of Mechanical and  
Aerospace  
Engineering  
Ithaca, NY 14853

Professor W.W. Willmarth  
The University of Michigan  
Department of Aerospace Engineering  
Ann Arbor, MI 48109

Professor A. Roshko  
California Institute of Technology  
Graduate Aeronautical Laboratories  
Pasadena, CA 91125

Professor J.T.C. Liu  
Brown University  
Division of Engineering  
Providence, RI 02912

Professor Patrick Leehey  
Massachusetts Institute of  
Technology  
Department of Ocean Engineering  
Cambridge, MA 02139

Professor Eli Reshotko  
Case Western Reserve University  
Department of Mechanical and  
Aerospace Engineering  
Cleveland, OH 44106

Dr. Steven A. Orszag  
Cambridge Hydrodynamics, Inc.  
P.O. Box 1403  
Princeton, NJ 08542

Professor Tuncer Cebeci  
California State University  
Mechanical Engineering Department  
Long Beach, CA 90840

Dr. C.W. Hirt  
University of California  
Los Alamos Scientific Laboratory  
P.O. Box 1663  
Los Alamos, NM 87544

Prof. Marshall P. Tulin  
Department of Mechanical and  
Environmental Engineering  
University of California at Santa  
Barbara  
Santa Barbara, CA 93106

Prof. Jin Wu  
College of Marine Studies  
University of Delaware  
Lewes, DE 19958

Dr. R.J. Hansen  
Code 5844  
Naval Research Laboratory  
Washington, DC 20375

Prof. S.G. Rubin  
Department of Aerospace  
Engineering and  
Applied Mechanics  
University of Cincinnati  
Cincinnati, OH 45221

Professor S.F. Shen  
Sibley School of Mechanical and  
Aerospace Engineering  
Cornell University  
Ithaca, NY 14850

Prof. J.E. Kerwin  
Department of Ocean Engineering  
Massachusetts Institute of  
Technology  
Cambridge, MA 01778

Prof. C.M. Ho  
Department of Aerospace  
Engineering  
University of Southern  
California  
University Park  
Los Angeles, CA 90007  
2 copies

Dr. Do C. Kwak  
Applied Computational  
Aerodynamics Branch  
NASA Ames Research Center  
M/S 202A-14  
Moffet Field, CA 94035

Prof. V.C. Patel  
Institute of Hydraulic Research  
The University of Iowa  
Iowa City, IA 52242

Prof. P.G. Saffman  
Department of Applied  
Mathematics  
California Institute of  
Technology  
Pasadena, CA 91125

Dr. N. Salvesen  
Science Applications, Inc.  
134 Holiday Court, Suite 318  
Annapolis, MD 21401

Prof. O.M. Phillips  
Department of Earth and  
Planetary Science  
Johns Hopkins University  
Baltimore, MD 21218

Prof. P.M. Naghdi  
Dept. of Mechanical Engineering  
University of California  
Berkeley, CA 94720

Dr. T.D. Taylor  
Applied Physics Laboratory  
Johns Hopkins University  
Baltimore, MD 21218

Prof. W.G. Tiederman  
School of Mechanical Engineering  
Purdue University  
West Lafayette, IN 47907

Prof. R.W. Yeung  
Dept. of Naval Architecture  
and Offshore Engineering  
University of California  
Berkeley, CA 94720  
3 copies

Prof. R.L. Street  
Dept. of Civil Engineering  
Stanford University  
Stanford, CA 94305

Prof. W.R. Schowalter  
Dept. of Chemical Engineering  
Princeton University  
Princeton, NJ 08540

Prof. T. Maxworthy  
Dept. of Mechanical Engineering  
University of Southern California  
University Park  
Los Angeles, CA 90089-0192

Prof. J. Schetz  
Dept. of Aerospace & Ocean  
Engineering  
Virginia Polytechnic Institute and  
State University  
Blacksburg, VA 24061  
2 copies

Prof. D. Rockwell  
Dept. of Mechanical Engineering  
and Mechanics  
Lehigh University  
Bethlehem, PA 18015

Prof. J.B. Keller  
Dept. of Mathematics  
Stanford University  
Stanford, CA 94305

Prof. A.J. Acosta  
Dept. of Mechanical Engineering  
California Institute of Technology  
Pasadena, CA 91125

Prof. J.N. Newman  
Dept. of Ocean Engineering  
Massachusetts Institute of  
Technology  
Cambridge, MA 01778

Prof. J.E. Kerwin  
Dept. of Ocean Engineering  
Massachusetts Institute of  
Technology  
Cambridge, MA 01778

Dr. S.J. Shamroth  
Scientific Research Associates,  
Inc.  
P.O. Box 498  
Glastonburg, CT 06033

Prof. W.S. Vorus  
Dept. of Naval Architecture and  
Marine Engineering  
University of Michigan  
Ann Arbor, MI 48109

Prof. A.H. Nayfeh  
Dept. of Engineering Sciences &  
Mechanics  
Virginia Polytechnic Institute and  
State University  
Blacksburg, VA 24061

Prof. T.Y. Wu  
Dept. of Engineering Science  
California Institute of Technology  
Pasadena, CA 91125

Prof. C.C. Mei  
Dept. of Civil Engineering  
Massachusetts Institute of  
Technology  
Cambridge, MA 02139

Prof. S.A. Berger  
Dept. of Mechanical Engineering  
University of California  
Berkeley, CA 94720

Prof. J.W. Miles  
Dept. of Geophysics  
University of California  
La Jolla, CA 92093

Dr. J.H. Duncan  
Flow Research Company  
1320 Fenwick Lane, Suite 401  
Silver Spring, MD 20910

Prof. C.E. Brennen  
Dept. of Mechanical Engineering  
California Institute of Technology  
Pasadena, CA 91125

Prof. R.F. Beck  
Dept. of Naval Architecture and  
Marine Engineering  
University of Michigan  
Ann Arbor, MI 48109

END  
DATE  
FILMED  
MARCH  
1988  
DTIC